Computer Methods in Applied Mechanics and Engineering 427 (2024) 117077

Contents lists available at ScienceDirect

Comput. Methods Appl. Mech. Engrg.

journal homepage: www.elsevier.com/locate/cma

An integrated heart–torso electromechanical model for the simulation of electrophysiological outputs accounting for myocardial deformation

Elena Zappon [a,b,*], Matteo Salvador [a,c], Roberto Piersanti [a], Francesco Regazzoni [a], Luca Dede' [a], Alfio Quarteroni [e,d,1]

[a] MOX - Dipartimento di Matematica, Politecnico di Milano, Milan, Italy
[b] Gottfried Schatz Research Center Biophysics, Medical University of Graz, Graz, Austria
[c] Institute for Computational and Mathematical Engineering, Stanford University, CA, USA
[d] Politecnico di Milano, Milan, Italy
[e] École Polytechnique Federale de Lausanne, Lausanne, Switzerland

ARTICLE INFO

Keywords:
Heart–torso model
Electrocardiograms
Cardiac electromechanics
Multiphysics modeling
Body surface potential maps

ABSTRACT

When generating in-silico clinical electrophysiological outputs, such as electrocardiograms (ECGs) and body surface potential maps (BSPMs), mathematical models have relied on single physics, i.e. of the cardiac electrophysiology (EP), neglecting the role of the heart motion. Since the heart is the most powerful source of electrical activity in the human body, its motion dynamically shifts the position of the principal electrical sources in the torso, influencing electrical potential distribution and potentially altering the EP outputs. In this work, we propose a computational model for the simulation of ECGs and BSPMs by coupling a cardiac electromechanical model with a model that simulates the propagation of the EP signal in the torso, thanks to a flexible numerical approach, that simulates the torso domain deformation induced by the myocardial displacement. Our model accounts for the major mechano-electrical feedbacks, along with unidirectional displacement and potential couplings from the heart to the surrounding body. For the numerical discretization, we employ a versatile intergrid transfer operator that allows for the use of different Finite Element spaces to be used in the cardiac and torso domains. Our numerical results are obtained on a realistic 3D biventricular-torso geometry, and cover both cases of sinus rhythm and ventricular tachycardia (VT), solving both the electromechanical-torso model in dynamical domains, and the classical electrophysiology-torso model in static domains. By comparing standard 12-lead ECG and BSPMs, we highlight the non-negligible effects of the myocardial contraction on the EP-outputs, especially in pathological conditions, such as the VT.

1. Introduction

Computer-based simulations in cardiac electrophysiology (EP) have significantly advanced over the past decade [1–5]. Among the clinically reproducible outputs of interest, the electrocardiogram (ECG) is a non-invasive and easy-to-achieve recording of

* Corresponding author at: Gottfried Schatz Research Center Biophysics, Medical University of Graz, Graz, Austria.
E-mail addresses: elena.zappon@medunigraz.at (E. Zappon), msalvad@stanford.edu (M. Salvador), roberto.piersanti@polimi.it (R. Piersanti), francesco.regazzoni@polimi.it (F. Regazzoni), luca.dede@polimi.it (L. Dede'), alfio.quarteroni@polimi.it (A. Quarteroni).
[1] Professor Emeritus.

https://doi.org/10.1016/j.cma.2024.117077
Received 9 February 2024; Received in revised form 15 May 2024; Accepted 17 May 2024
Available online 31 May 2024

cardiac EP, and serves in clinical practice as a default tool. In computational cardiology, the ability of accurately reproduce ECG waveform represents a footprint of quality standard [6–8]. This alignment underscores the potential for simulated models to closely mirror real-world physiological processes [6,9–13], including cardiac diseases such as myocardial infarction [14] and ventricular tachycardia (VT) [15,16]. On the other hand, body surface potential maps (BSPMs) are not often utilized in clinical settings, but provide a detail description of bioelectric signals spanning the entire thorax. This allows for a more comprehensive analysis of the electrophysiological condition in contrast to the standard ECG. BSPMs have found application in patients affected by a broad range of pathologies, including myocardial infarction, ventricular hypertrophy, and cardiac arrhythmias [17,18]. From a computational perspective, BSPMs have been used in studying ablation targets for atrial arrhythmias [19–21] and examining the effects of drug-induced conditions [22].

Cardiac EP corresponds to the synchronized depolarization and repolarization of cardiomyocytes. The tissue depolarization then initiates the mechanical contraction, and therefore deformation, of the heart. Since the heart is the main active source of the electrical field in the human body [23,24], its deformation leads the potential to (i) influence the transmission of the EP signal within the cardiac tissue itself and (ii) shifts the origins of the electrical field with respect to the body surface, that instead is almost fixed during a single heart beat. Specifically, this last occurrence can lead to changes in the direction of the EP signal propagation throughout the torso, consequently affecting the ECGs and the BSPMs. Indeed, numerous studies have demonstrated that differences in heart location [25–30] and dimensions [26,31,32] in the torso can significantly impact the propagation of the electrical signal within the human body and the EP clinical outputs. This means that the cardiac contraction, determining large deformation and, even, a twist of the heart tissue, may contribute to the genesis of the ECG signals and BSPMs.

A mathematical model for the generation of EP clinical outputs typically involves two key components: a cardiac electrophysiological model, such as the Bidomain [23,33–36], the Monodomain [23,35,37], or the Eikonal one [38–41], and a model to calculate the ECG and BSPMs from the electrical signal propagation through the torso [23,35]. The latter can be simulated using the lead-field model [12,42,43], enabling the direct computation of ECG leads through time, or by solving a Laplace problem [33,35,44–46], allowing the computation of ECGs and BSPMs as post-processing of the problem solution. These models are usually approximated by means of the Finite Element methods [23]. An alternative is represented by the boundary element method (BEM) [47–50]. Regardless of the chosen representation, the electrophysiology-torso models consider the heart as a static domain – default anatomy is that of the heart in diastasis configuration – embedded in a corresponding static torso domain, therefore neglecting the dynamic cardiac deformations.

The impact of cardiac mechanical displacement on the EP has been explored in some preliminary studies by de Oliveira et al. [51] and Favino et al. [52], who employ an electromechanical model (EM) in place of an EP one, yet only simulating electrogram signals (EGMs). In the work of Smith et al. [53], EP signals obtained by employing dynamic heart–torso domains depending on cardiac displacement are analyzed, albeit in a 2D context. Conversely, simulations in 3D domains were conducted in studies by Keller et al. [54], Wei et al. [55], and Xia et al. [56], deriving the displacement data from MRI images. Moreover, different electromechanical modeling approaches yield very different outcomes. Indeed, when accounting for the EGMs in 2D models, Wei et al. [55] and Xia et al. [56] observed only a marginal change in torso potential due to cardiac displacement. Smith et al. [53] noted instead a significant impact of myocardial contraction on the ECGs, particularly evident in the precordial leads and T wave. Keller et al. [54], on the other hand, reported a substantial influence of ventricular displacement on lead II. The computation of ECGs and BSPMs in dynamic heart and torso domains has been instead explored only in [57], where the authors incorporate the computed myocardial displacement in the EP outputs simulation by remeshing a portion of the torso for each new cardiac configuration. The procedure of [57] is tested only in sinus rhythm conditions. However, in [58,59], the authors emphasize that when pathological conditions and rhythm disorders, such as VT, arise, mechano-electric feedbacks (MEFs) may have a strong effect on the EP signal propagation in the heart and, thus, on the overall EP outputs. A cardiac electromechanical model for studying drug-induced VT was developed in [60], where the authors also computed pseudo-ECGs. However, they consider only a unidirectional coupling from the electrophysiological model to the mechanical model. Hence, although the mechanical solution is influenced by the electrophysiological one, the EP is not affected by the MEFs. Furthermore, pseudo-ECGs are generated using a projection approach that does not incorporate a realistic torso surrounding the heart; instead, it assumes that the electrodes are fixed at a certain distance from the heart. Moreover, at each time instant of the simulation, the changes in the distance between the heart mesh nodes and the electrodes due to the cardiac displacement are not considered, since the heart is still treated as static.

In this work, we propose a 3D multi-physics and multi-scale model for the computation of EP clinical outputs for a moving heart. We couple the cardiac electromechanical model presented in [61,62], with a Laplace problem in the torso [33], and employing a lifting technique to account for the dynamic deformation of the torso domain due to the myocardial displacement (see Fig. 1). The resulting electro-mechanical-torso (EMT) model is an effective alternative of the one presented in [57]. The EM model of [61,62] includes an accurate description of cardiac EP, extended to represent extracellular potential, passive mechanics, ventricular active contraction, and a reduced-order representation of the circulatory system, fully coupled with the mechanical model of the heart. Moreover we also account for MEFs, fibers-stretch and fibers-stretch-rate feedbacks — which have been found to be important to regulate the electromechanical behavior of the heart [61]. Finally, the cardiac mechanical displacement is used as boundary conditions to solve a linear elasticity lifting model in the torso domain. The solution of this problem determines the displacement responsible for the online deformation of the torso domain. The Laplace model that accounts for the propagation of the cardiac extracellular potential on the torso [33] is then solved within the deformed torso domain, and the ECGs and BSPMs are post-processed from the torso solution.

Concerning the numerical discretization, we extend the accurate and efficient segregated–intergrid–staggered scheme employed in [61,63] to include the torso models. The implemented scheme offers flexibility and allows to prescribe an arbitrary and time-independent displacement to either, or both, cardiac and torso problems. Consequently, we gain the capability to simulate the EMT

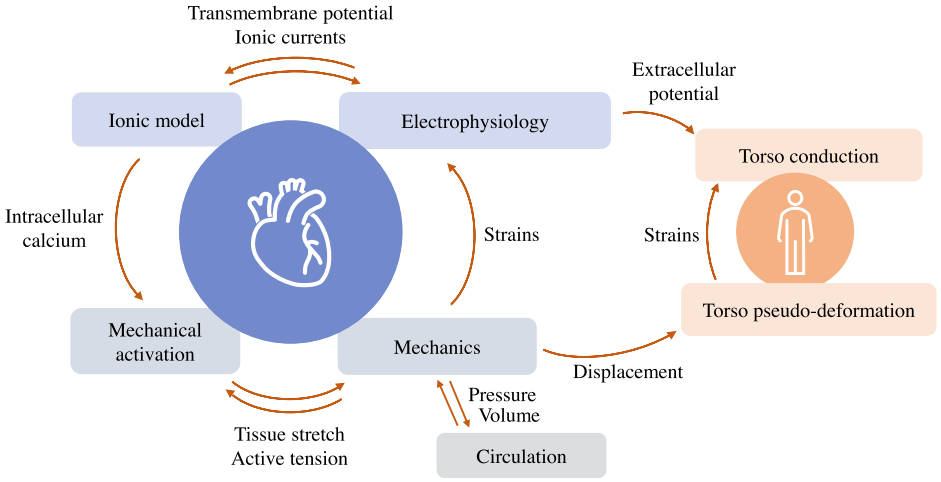

Fig. 1. Schematic representation of the implemented electro-mechano-torso model.

model in moving domains while also safely addressing the EMT solution in static domains — thus recovering the static EP-torso model usually employed for computing ECGs and BSPMs. This framework accommodates hybrid scenarios, such as a static heart with a moving torso, or a moving heart with a static torso. This facilitates the separate analysis of (i) the effects of myocardial deformation on EP propagation within the heart and, consequently, on the ECG, and (ii) of the impact of shifting the torso domain shape, and thus the position of the electrical sources in the body, according to the myocardial displacement. The proposed computational framework leverages high-performance computing to enable large-scale simulations, making use of the C++ finite element library `life`^{x} [64–66].

We perform numerical simulations using 3D realistic biventricular and torso geometries. To assess the impact of myocardial deformation on the EP outputs, we compare ECGs and BSPMs obtained from the EMT solution in various configurations: dynamic heart–torso domains, static heart–torso domains, and the hybrid configurations. We simulate both healthy and pathological scenarios, specifically replicating VT induced by idealized scar and gray zones on the biventricular septum, following [58].

The work is organized as follows: in Section 2 we provide the description of EMT mathematical model; in Section 3 we briefly describe our numerical framework; in Section 4 we present the numerical results obtained with the proposed EMT model; finally, in Sections 5 and 6 we discuss our key finding and implications of the study, and draw our conclusions.

2. Mathematical model

Let $\Omega_H \subset \mathbb{R}^3$ and $\Omega_T \subset \mathbb{R}^3$ denote two open, time dependent bounded domains, representing the spaces occupied by the human heart and the rest of the human body surrounding Ω_H, respectively, at each time instance of the heartbeat. Hereon, Ω_H will be represented by a basal biventricular geometry, i.e. a biventricular geometry cut below the cardiac valves (see Fig. 2). To prevent undesirable deformation of the finite elements in Ω_T around the edges of the cardiac basal plane, and consequent convergence issues of the numerical solver, the internal volume of the ventricular chambers is further isolated from the rest of Ω_T by sealing the ventricular base with two thin layers of flexible non-conductive tissue, which we refer to as caps and denote by Ω_C (see Fig. 2).

Remark 1. While caps do not constitute physiological structures within the heart, in this work they are non-conductive entities from an electrophysiological perspective, and passive tissue from the mechanical standpoint. Furthermore, the applied boundary conditions at their edges ensure synchronized movement with both cardiac tissue and the surrounding torso, without affecting the motion of either heart or torso tissue. Consequently, they do not contribute to the propagation of electrical signals or the deformation of heart and torso domains, thereby having no impact on the generation of ECGs and BSPMs. These caps can be, therefore, entirely disregarded whenever such steep angles are not present in the cardiac domain.

The boundary $\partial\Omega_H$ is further split into the left endocardial surface $\Gamma_H^{\text{endo,LV}}$, the right endocardial surface $\Gamma_H^{\text{endo,RV}}$, the epicardial surface Γ_H^{epi}, and the base Γ_H^{base}. Additionally, we denote:

- $\Gamma_C^{\text{endo,RV}}$ and $\Gamma_C^{\text{endo,LV}}$ as the portions of $\partial\Omega_C$ directed towards the right and left ventricular chambers, respectively.
- $\Gamma_C^{\text{epi,RV}}$ and $\Gamma_C^{\text{epi,LV}}$ as the portions of $\partial\Omega_C$ directed towards the torso.

For the sake of notation, in the rest of the paper we will identify the union of different portions of the boundary of Ω_T, Ω_H and Ω_C as:

- $\Gamma = \partial\Omega_T \cap (\partial\Omega_H \cup \partial\Omega_C)$ to represent the interface between the torso domain Ω_T and the heart-caps volume Ω_H-Ω_T.

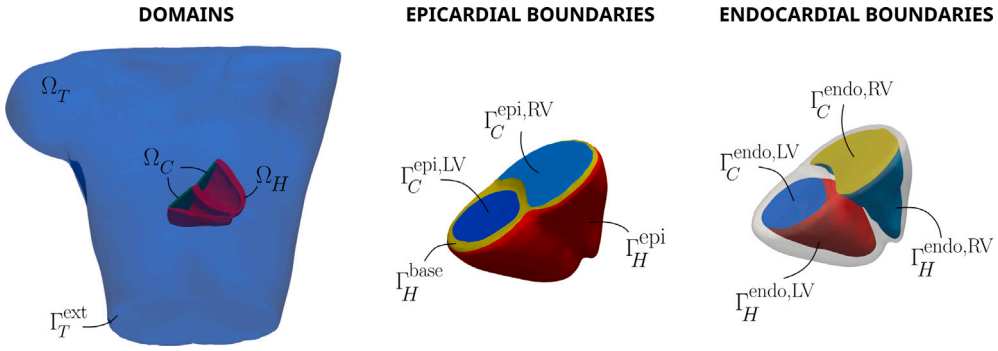

Fig. 2. Left: Domains Ω_T (torso), Ω_H (biventricular geometry), and Ω_C (caps). The external surface of the torso is indicated as Γ_T^{ext}. Center and right: partitioned of the boundary $\partial\Omega_H$ in epicardium $\Gamma_H^{\text{epi,LV}}$ and $\Gamma_H^{\text{epi,RV}}$, base Γ_H^{base}, and left and right endocardium $\Gamma_H^{\text{endo,LV}}$ and $\Gamma_H^{\text{endo,RV}}$. The portion of $\partial\Omega_C$ representing the surface directed to the torso, both left and right $\Gamma_C^{\text{epi,LV}}$ and $\Gamma_C^{\text{epi,RV}}$, and directed to the cardiac endocardium, both left and right $\Gamma_C^{\text{endo,LV}}$ and $\Gamma_C^{\text{endo,RV}}$, are also indicated.

- $\Gamma^{\text{RV}} = \Gamma_H^{\text{endo,RV}} \cup \Gamma_C^{\text{endo,RV}} \cup \Gamma_C^{\text{epi,RV}}$ for domain boundaries related to the right ventricle.
- $\Gamma^{\text{LV}} = \Gamma_H^{\text{endo,LV}} \cup \Gamma_C^{\text{endo,LV}} \cup \Gamma_C^{\text{epi,LV}}$ for domain boundaries related to the left ventricles.

Finally, the external surface of the torso is defined as Γ_T^{ext} (see Fig. 2).

For each domain, the deformation is moreover computed starting from a *static reference configuration* denoted by $\Omega^0_{\{H,T,C\}}$.

We denote by t the time variable. To keep the notation light, in this work t is usually omitted.

The EMT model is obtained by coupling the EM model presented in [61,62] (including electrophysiology, active force generation, passive mechanics, and cardiovascular hemodynamics) with a torso domain deformation model, and a torso passive conduction model. Specifically, the EMT model features the following unknowns:

$$\begin{aligned}
&u : \{\Omega_H^0 \cup \Omega_C^0\} \times [0,T] \to \mathbb{R}, && u_e : \{\Omega_H^0 \cup \Omega_C^0\} \times [0,T] \to \mathbb{R},\\
&\boldsymbol{\omega} : \{\Omega_H^0 \cup \Omega_C^0\} \times [0,T] \to \mathbb{R}^{n_{\boldsymbol{\omega}}}, && \mathbf{z} : \Omega_H^0 \times [0,T] \to \mathbb{R}^{n_{\mathbf{z}}},\\
&\mathbf{d}_H : \{\Omega_H^0 \cup \Omega_C^0\} \times [0,T] \to \mathbb{R}^3, && \mathbf{c} : [0,T] \to \mathbb{R}^{n_{\mathbf{c}}},\\
&p_i : [0,T] \to \mathbb{R},\ i \in \{RV, LV\}, && \mathbf{d}_T : \Omega_T^0 \times [0,T] \to \mathbb{R}^3,\\
&u_T : \Omega_T^0 \times [0,T] \to \mathbb{R}, &&
\end{aligned} \tag{1}$$

where u and u_e are the transmembrane and extra-cellular potentials, respectively, $\boldsymbol{\omega}$ represents the vector of the ionic variables, $\mathbf{z}$ is the vector of state variables of the force generation model, $\mathbf{d}_H$ is the cardiac mechanical displacement, here extended to include the caps, $\mathbf{c}$ is the state vector of the circulation model, p_{RV} and p_{LV} are the blood pressures inside the biventricular domain, $\mathbf{d}_T$ is the displacement of the torso domain, and u_T is the electric potential in the torso.

In the following sections, we present a brief description of the models involved in the cardiac EM model is presented, and a detailed one for the torso model. A complete description of the EM model can be found in Appendix.

2.1. Cardiac electrophysiology

We simulate the electrical excitation and propagation in the cardiac tissue by solving the Monodomain model [23,35,37] coupled with the ten Tusscher–Panfilov (TTP06) ionic model [67] in the reference configuration, computing the transmembrane potential u and the ionic variables $\boldsymbol{\omega}$ and $\mathbf{z}$.

Vectors $\mathbf{f}_0$, $\mathbf{s}_0$, and $\mathbf{n}_0$, denoting the fiber, sheet and sheet-normal directions, are computed using the Laplace–Dirichlet-Rule-Based-Methods (LDRBMs) outlined in [68]. A gradual transmural twist from 60° at the endocardium to −60° at the epicardium is considered for the fiber orientations. Tissue parameters are tuned to achieve conduction velocities of 0.6, 0.4, and 0.2 m/s in the longitudinal $\mathbf{f}_0$, transverse $\mathbf{s}_0$, and normal $\mathbf{n}_0$ directions of cardiac myocytes, respectively [68].

The myocardial conduction system is surrogated by a transmembrane current applied to five activation points on the endocardial surfaces and a thin, fast endocardial layer, able to mimic physiological activation [69,70]. Activation impulses, along with the velocity of the fast endocardial layer, are calibrated to generate physiological ECG waves, as described in [33].

To account for the tissue stretch computed by the mechanical model, the deformation gradient tensor $\mathbf{F}_H = \mathbf{I} + \nabla\mathbf{d}_H$ and the corresponding Jacobian $J_H = \det(\mathbf{F}_H) > 0$ are included in the diffusion term of the Monodomain model, as well as in the definition of the anisotropic diffusion tensor (we refer the reader to [62,63] and Appendix for a detailed description of the Monodomain formulation).

The extracellular potential u_e, which is assumed to be the only electrical potential extending outside the heart and into the rest of the human body [23,71], is obtained from the transmembrane potential u by solving the following Laplace problem [33,44]:

$$\begin{cases}
-\nabla\cdot(J_H\mathbf{F}_H^{-1}(\mathbf{D}_i+\mathbf{D}_e)\mathbf{F}_H^{-T}\nabla u_e) = \nabla\cdot(J_H\mathbf{F}_H^{-1}\mathbf{D}_i\mathbf{F}_H^{-T}\nabla u) & \text{in } \{\Omega_H^0 \cup \Omega_C^0\}\times(0,T], \quad (2b)\\
(J_H\mathbf{F}_H^{-1}(\mathbf{D}_i+\mathbf{D}_e)\mathbf{F}_H^{-T}\nabla u_e)\mathbf{n}_H = -(J_H\mathbf{F}_H^{-1}\mathbf{D}_i\mathbf{F}_H^{-T}\nabla u)\mathbf{n}_H & \text{on } \{\partial\Omega_H^0 \cup \partial\Omega_C^0\}\times(0,T]. \quad (2c)
\end{cases}$$

In the above equations, $\boldsymbol{D}_i$ and $\boldsymbol{D}_e$ are the intra-cellular and extra-cellular diffusion tensors, respectively, obtained for each $t \in (o, T)$ as follows:

$$\boldsymbol{D}_{i,e} = \sigma_{\ell}^{i,e} \frac{\mathbf{F}_H \mathbf{f}_0 \otimes \mathbf{F}_H \mathbf{f}_0}{\|\mathbf{F}_H \mathbf{f}_0\|^2} + \sigma_t^{i,e} \frac{\mathbf{F}_H \mathbf{s}_0 \otimes \mathbf{F}_H \mathbf{s}_0}{\|\mathbf{F}_H \mathbf{s}_0\|^2} + \sigma_n^{i,e} \frac{\mathbf{F}_H \mathbf{n}_0 \otimes \mathbf{F}_H \mathbf{n}_0}{\|\mathbf{F}_H \mathbf{n}_0\|^2},$$

where $\sigma_{\ell,t,n}^{i,e}$ are the conduction coefficients of the cardiac tissue in the fiber, sheet, and sheet-normal directions. Hereon, the combination of the Monodomain model with problem (2) is referred to as Pseudo-bidomain model.

Remark 2. In this work, we do not model the effect of transmural and apico-basal cell heterogeneity. Such heterogeneity, that corresponds to variations in action potential durations among cardiac cells, is ultimately responsible for the generation of a physiological T wave. Consequently, the simulated T wave of Section 4 may exhibits non-physiological behavior. Despite this limitation, observed variations in the T wave due by myocardial contraction are independent from this heterogeneity, and can be therefore equally appreciated and investigated through this study.

2.2. Cardiomyocytes active contraction

Cardiomyocyte active contraction bridges electrophysiology and passive mechanics, as it captures the contraction of sarcomeres resulting from fluctuations in calcium concentration $[Ca^{2+}]_i$, simulated by the ionic model, and the myocardial displacement $\mathbf{d}_H$, provided by the mechanical model. To model the active force generated within the cardiac muscle, we employ the mean-field version of the models proposed in [72], denoted as RDQ model. These models have been shown to efficiently describe the regulatory and contractile proteins and their dynamics, ensuring biophysical accuracy [62,73].

The output of the RDQ models is the active tension generated at the microscale, denoted as T_a. Furthermore, an active stress approach is used to manage mechanical force generation, receiving intracellular calcium as input from the ionic model.

2.3. Passive and active mechanics

To describe the tissue stress–strain relationship, the cardiac and caps tissue is assumed to be nearly incompressible, anisotropic, and hyperelastic [74,75]. The displacement $\mathbf{d}_H$ is therefore obtained by solving a momentum conservation equations endowed with proper boundary conditions. To account for the active mechanics, the Piola–Kirchhoff stress tensor is defined by an orthotropic active stress approach [76,77], with a strain energy term depending on the Usyk constitutive law [61,78].

The mechanical forces arising from the interaction between the epicardium and the pericardium [79–81] are enforced through generalized Robin boundary conditions applied to the epicardial surface $\Gamma_H^{\text{epi,RV}} \cup \Gamma_H^{\text{epi,LV}}$. Normal stress boundary conditions are employed on the endocardial surfaces and the boundaries of the cap directed towards the torso, that is on Γ^{RV} and Γ^{LV}, to model the pressure exerted by the blood. Energy-consistent boundary conditions, addressing the influence of the neglected portion of the heart, i.e. the atria, on the biventricular domain, are applied to Γ_H^{base} [62]. A detailed description of the cardiac mechanical models is given in Appendix.

2.4. Circulatory system and coupling conditions

The influence of the circulatory system on cardiac mechanics is simulated using the 0D closed-loop model proposed in [62,63], where other distinct parts of the circulatory system are represented by a series of resistor–inductor–capacitor circuits, the 0D cardiac chambers are characterized by time-varying elastance elements, and heart valves are simulated using non-ideal diodes.

The coupling of the 0D circulatory model with the 3D EM model is achieved by substituting the time-varying elastance elements representing the LV and RV in the circulatory model with their corresponding 3D EM descriptions with suitable volume-consistency coupling conditions [62]. For a more detailed description of the circulation model and the 3D–0D coupling conditions, we refer to Appendix.

2.4.1. VT modeling

VT is a rhythm disorder that is triggered by different cardiac dysfunctions. We define an idealized ischemia in the biventricular geometry in order to create a potential pathway for VT. In this manner, we investigate how the cardiac contraction may influence the generation of pathological ECGs.

Ischemia is mathematically modeled by defining myocardial regions with slow conduction properties, denoted by gray zones, and actual scars, respectively. To this end, following [59], we introduce a parameter $\mu = \mu(\mathbf{x}) \in [0, 1]$ in the definition of the anisotropic diffusion tensor:

$$\boldsymbol{D}_{i,e} = \mu\sigma_{\ell}^{i,e} \frac{\mathbf{F}_H \mathbf{f}_0 \otimes \mathbf{F}_H \mathbf{f}_0}{\|\mathbf{F}_H \mathbf{f}_0\|^2} + \mu\sigma_t^{i,e} \frac{\mathbf{F}_H \mathbf{s}_0 \otimes \mathbf{F}_H \mathbf{s}_0}{\|\mathbf{F}_H \mathbf{s}_0\|^2} + \mu\sigma_n^{i,e} \frac{\mathbf{F}_H \mathbf{n}_0 \otimes \mathbf{F}_H \mathbf{n}_0}{\|\mathbf{F}_H \mathbf{n}_0\|^2},$$

as well as in the TTP06 ionic model [58,82], able to selectively change the conduction properties of specific portion of the cardiac tissue. The parameter μ is 1 when representing healthy tissue, 0 for scar regions, whereas linear interpolation of $\mu \in [0.1, 1]$ can be used to simulate a continuous of gray zones. We refer to [58,59] for the description of EM models for ischemic cardiomyopathy. Moreover, since the cardiomyocytes active contraction model receives the intracellular calcium as input from the ionic model, which is dependent of μ, the differentiation between the healthy, scar, and gray zones is straightforward included in the cardiac mechanics.

2.5. Torso passive conduction and domain deformation

The computation of ECGs and BSPMs is obtained by solving a Laplace problem that models the torso as a passive conductor, as outlined in [33,44], with some modifications. Indeed, the conventional representation views the torso as a static domain. However, the mechanical contractions of the heart result in alterations to the heart–torso interface, affecting the torso domain around the heart. This geometrical deformation changes the amount of tissue through which u_e spreads, potentially influencing the ECG and BSPMs. Our model is therefore designed to account for this effect by (i) calculating a virtual deformation of the torso computational domain due to cardiac contraction and (ii) incorporating this deformation into the signal propagation model.

Remark 3. In this study, we aim to investigate the impact of cardiac displacement and the resulting changes in the orientation of electrical sources within the torso on EP outputs. In pursuit of these objectives, our modeling approach specifically focuses on dynamically deforming the domain Ω_T in response to myocardial contraction while avoiding the corresponding remeshing, rather than simulating the physiological deformation of the torso tissue surrounding the heart due to its movement. We refer to this non-physiological deformation of the torso as pseudo-deformation, and the corresponding displacement $\mathbf{d}_T$ as pseudo-displacement.

The pseudo-deformation of the torso domain caused by myocardial displacement is accounted for through the following linear elasticity problem, as described in [83,84]:

$$\begin{cases} -\nabla\cdot\boldsymbol{\sigma}(\mathbf{d}_T) = \mathbf{0} & \text{in } \Omega_T^0, \quad (3c)\\ \mathbf{d}_T = \mathbf{d}_H & \text{on } \Gamma, \quad (3d)\\ \mathbf{d}_T = \mathbf{0} & \text{on } \Gamma_T^{\text{ext}}. \quad (3e) \end{cases}$$

which computes the torso domain pseudo-displacement $\mathbf{d}_T$ induced by the cardiac deformation $\mathbf{d}_H$. In problem (3), $\boldsymbol{\sigma}$ represents the Cauchy stress tensor:

$$\boldsymbol{\sigma}(\mathbf{d}_T) = \lambda\ tr(\boldsymbol{\varepsilon}(\mathbf{d}_T))\mathbb{I} + 2\ \mu\ \boldsymbol{\varepsilon}(\mathbf{d}_T),$$

of the torso tissue, being tr the trace operator, λ and μ are the Lamé constants, $\mathbb{I}$ the identity matrix and $\boldsymbol{\varepsilon}$ the strain tensor:

$$\boldsymbol{\varepsilon}(\mathbf{d}_T) = \frac{1}{2}(\nabla\mathbf{d}_T + (\nabla\mathbf{d}_T)^T).$$

The Lamé constants are expressed in terms of the Young's modulus E and of the Poisson's modulus ν according to the following formulation:

$$\lambda = \frac{E}{2(1+\nu)}, \qquad \mu = \frac{E\nu}{(1+\nu)(1-2\nu)},$$

enabling a direct description of the strain and deformation properties of the material under consideration.

The pseudo-displacement $\mathbf{d}_T$ is utilized to calculate the corresponding deformation gradient tensor $\mathbf{F}_T$ and Jacobian J_T. We assume that $\tilde{u}_T$ is the extracellular potential in the torso configuration at a given time t, obtained by solving the classical Laplace problem:

$$\begin{cases} -\nabla\cdot(\mathbf{D}_T\nabla\tilde{u}_T) = 0 & \text{in } \Omega_T(t),\\ (\mathbf{D}_T\nabla\tilde{u}_T)\cdot\tilde{\mathbf{n}}_T = 0 & \text{on } \Gamma_T^{\text{ext}},\\ \tilde{u}_T = \tilde{u}_e & \text{on } \Gamma(t), \end{cases} \quad (4)$$

where $\mathbf{D}_T$ is the isotropic diffusion tensor in the torso, and is the cardiac extracellular potential at time t. Following the same procedure presented in [71,85] for the electrophysiological model 2.1, after the pull-back in the reference configuration Ω_T^0, we compute the electrical potential u_T on the reference configuration Ω_T^0 by solving the following problem:

$$\begin{cases} -\nabla\cdot(J_T\mathbf{F}_T^{-1}\mathbf{D}_T\mathbf{F}_T^{-1}\nabla u_T) = 0 & \text{in } \Omega_T^0,\\ (J_T\mathbf{F}_T^{-1}\mathbf{D}_T\mathbf{F}_T^{-1}\nabla u_T)\cdot\mathbf{n}_T = 0 & \text{on } \Gamma_T^{\text{ext}},\\ u_T = u_e & \text{on } \Gamma, \end{cases} \quad (5)$$

where $\mathbf{n}_T$ is the unit outward normal to Ω_T^0.

Problem (5) yields the electric field generated by the heart throughout the entire torso over time. BSPMs are subsequently derived in post-processing as $u_{T_{|\Gamma_T^{\text{ext}}}}$. The traditional leads of the 12-lead ECG system are computed by aggregating the values of $u_T(\mathbf{x}_e)$ over time, where $\mathbf{x}_e$ denotes the spatial position of the electrodes on the body surface (we refer the reader to Appendix for a detailed description of the leads computation). Our strategy, by computing the pullback of the moving torso problem in the reference domain, allows for solving the problem on a reference static mesh, thus preventing the need for continuously remeshing the area surrounding the heart, as done e.g. in [57].

2.6. Reference configurations and initial conditions

Cardiac – and corresponding torso – geometries are derived from the analysis of in vivo medical images, that are typically acquired during the diastasis phase. The blood pressure acting on the endocardium introduces stress into the resulting geometries. However, the reference configurations $\Omega_{H,T,C}^0$ represent a stress-free state.

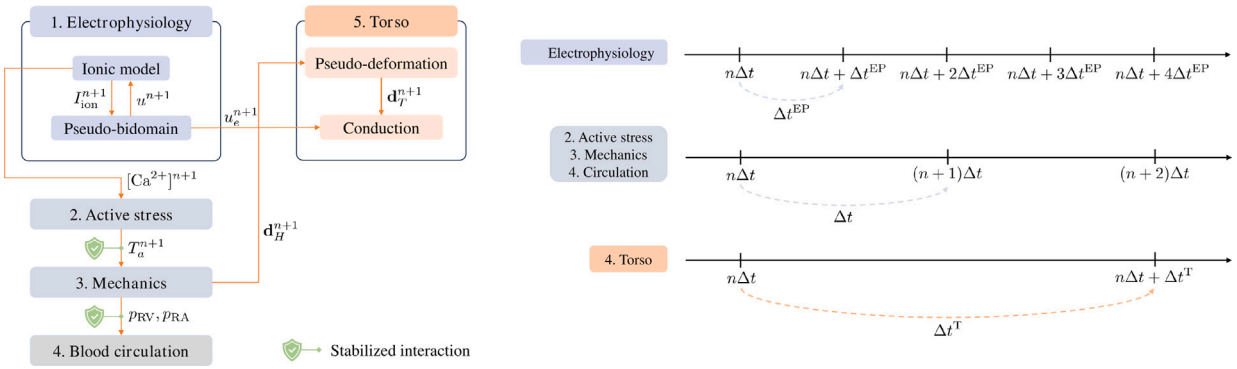

Fig. 3. Time-advancing scheme for the coupled EMT model. The number referred to the computational order for a single time step t_n.

While the cardiac geometry undergoes deformation due to active cardiac mechanical dynamics, both the caps and the torso deformations are passively induced by the cardiac displacement. Furthermore, while the entire domain of the caps deforms under the effect of cardiac deformation, the torso domain is altered only at the heart–torso interface. This same dynamic interaction among the three domains is considered in the computation of their respective reference configurations.

Assuming that the imaging of the cardiac geometry $\tilde{\Omega}_H$ refers to a diastasis configuration, the cardiac reference configuration is obtained by solving the inverse problem presented in [63]. As the motion of the caps depends on the blood pressure in the cardiac chambers, the inverse problem of [63] is solved in a unique domain $\tilde{\Omega}_H \cup \tilde{\Omega}_C$, constructed by incorporating the artificial caps $\tilde{\Omega}_C$ into the cardiac imaging configuration $\tilde{\Omega}_H$.

Once the reference configurations Ω_H^0 and Ω_C^0 have been computed, the torso reference configuration Ω_T^0 is constructed by inserting $\Omega_H^0 \cup \Omega_C^0$ into the imaging torso domain $\tilde{\Omega}_T$, replacing $\tilde{\Omega}_H$.

Initial conditions for the electromechanical problem are set as in [62], by surrogating the 3D–0D EM problem with a 0D emulator able to efficiently compute the model parameters at limit cycle [86].

3. Numerical framework

The discretization strategy employed for numerically solving the EMT problem is derived by extending the segregated–intergrid–staggered numerical scheme presented in [62] to incorporate the pseudo-deformation of the torso domain and passive conduction. This scheme allows to combine the static and/or dynamic configurations for both the heart and the torso, thereby distinguishing between the effects of cardiac motion and torso pseudo-deformation on the ECG and BSPMs.

Details regarding time and space discretization strategies are provided in Section 3.1, while the possible combinations of cardiac and torso domain configurations are outlined in Section 3.2.

3.1. Time and space discretizations

The time interval $[0, T]$ is divided into sub-intervals $[t_i, t_{i+1}]$ for $i = 0, 1, \dots, N$, where $t_0 = 0$ and $t_N = T$, ensuring a uniform time step size of Δt for all i. Hereon, we denote the approximation of the solution variables (1) at a given time step t_n by the superscript n, e.g. $u(t_n) \approx u^n$.

The staggered scheme presented in [62] to solve the coupled EM model is extended to include the pseudo-deformation of the torso domain (3) and the propagation of the cardiac extracellular potential u_e in the torso domain (5) as final step of the simulation, as shown in Fig. 3.

The scheme involves solving different subproblems separately, using explicit coupling when stability is not a concern. This allows for choosing different time steps for the cardiac EP, mechanics, and torso models. The reference timestep Δt is used for the solution of the cardiomyocytes active force generation and the cardiac mechanics. Electrophysiology has a faster dynamics with respect to the other models, requiring a smaller timestep to ensure an accurate solution. Therefore, a timestep $\Delta t^{\mathrm{EP}} = \Delta t / N_{\mathrm{EP}}$, with $N_{\mathrm{EP}} \in \mathbb{N}$, is introduced. Cardiac electrical outputs, such as the ECGs and the BSPMs, can be computed less frequently. Indeed, a third timestep $\Delta t^{\mathrm{T}} = N_{\mathrm{T}} \Delta t$, with $N_{\mathrm{T}} \in \mathbb{N}$, is introduced for this purpose.

Time derivatives are approximated using Finite Difference schemes [87]. The cardiac electrophysiology model is solved using the Backward Differentiation Formula of order 2 (BDF2). An implicit–explicit (IMEX) scheme is adopted to treat the diffusion term implicitly and the ionic and reaction terms explicitly [61,88]. Mechanical activation and mechanics are solved with a BDF1 scheme, employing an explicit method for the cardiomyocyte contraction problem and a fully implicit scheme for the cardiac mechanical model. The circulation model is finally solved explicitly with a Runge–Kutta method of order 4 [61].

Remark 4. The torso problem presented in Section 2.5 is formally time-independent. Since the boundary conditions of (3) and (5) depend on cardiac quantities varying over time, the solution of the torso problems inherits time-dependency from the cardiac EM models. However, from a numerical standpoint, no time discretization strategies are required for the torso problems.

Table 1
Sketch of the cardiac and torso domain configurations used in the EMT simulations. The two domains can be either in a static configuration – by prescribing a time-independent $\mathbf{d}_H$ - or in a moving configuration – dynamically computing $\mathbf{d}_H$. The colors of the diagonal lines refer to the ECG traces of Section 4.

Heart \ Torso	Static configuration	Moving configuration
Static configuration	No MEFs / No MEFs	No MEFs / MEFs
Moving configuration	No MEFs / MEFs	No MEFs / MEFs

The three domains Ω_H^0, Ω_C^0, and Ω_T^0 are spatially discretized on tetrahedral meshes conforming at the domain interfaces. The electrophysiology model is discretized in space using piecewise quadratic finite elements $\mathbb{P}_2$ [89,90], which have been shown in [91] to provide improved accuracy with a lower number of degrees of freedom compared to $\mathbb{P}_1$ linear elements for cardiac electrophysiology. Linear finite elements $\mathbb{P}_1$ are used for the mechanical activation problem, active and passive mechanics, and torso problems. An efficient intergrid transfer operator is finally used to evaluate the feedback between EP and other physics.

3.2. Combining static and dynamic heart and torso configurations

Our numerical framework provides not only flexibility in terms of spatial and time discretizations, but allows the exploration of various electrophysiological and torso domain combined configurations. The comprehensive representation of the cardiac EM phenomena encompasses both the dynamic displacement of the heart and the torso domain.

Our numerical scheme facilitates this analysis by allowing the prescription of an arbitrary, time-independent displacements $\mathbf{d}_H$. This static displacement can be utilized:

- to compute a non-varying deformation tensor $\mathbf{F}_H$ for the Pseudo-bidomain model, simulating cardiac EP on a static configuration, which corresponds to the simulation of the cardiac electrophysiology without mechanical feedback.
- as a boundary condition for the linear elasticity problem (3) describing torso pseudo-deformation, thus equivalently simulating the torso as a passive conductor in a static domain.

Employing a time-independent $\mathbf{d}_H$ also corresponds to refraining from using the MEFs on either the cardiac or torso domain. This enables simulation of the EMT model under various scenarios on:

1. both cardiac and torso moving domains, i.e. the most complete representation
2. both cardiac and torso static domains, recovering the static EP-torso model typically used for computing ECGs and BSPMs
3. a static heart with a moving torso
4. a moving heart with a static torso.

The hybrid configurations 3. and 4. allow the analysis of (i) the effects of myocardial deformation on EP propagation within the heart and, consequently, on the ECG and BSPMs (equivalently reading Table 1 by columns), and (ii) the impact of shifting the heart–torso interface and thus varying the torso domain according to the myocardial displacement (equivalently reading Table 1 by rows).

4. Numerical results

We present the results obtained using our EMT model and numerical framework are presented and discussed. The EMT model was use to analyze two scenarios: the first representing healthy conditions, and the second simulating VT.

The organization of this section is as follows: the volumetric models and baseline parameters common to both test cases are presented in Section 4.1, the baseline simulations representing a healthy patient are displayed in Section 4.2, and the results for VT simulations are shown in Section 4.3.

4.1. Numerical simulation settings

The cardiac biventricular model is based on the Zygote Solid 3D Heart Model [92], which is an anatomically accurate CAD model of the entire human heart reconstructed from high-resolution CT scans. It represents a healthy male subject from the 50th percentile of the United States population. The original model has been processed to fit the domain described in Section 2. The biventricular geometry is cut below the valves to generate a basal biventricular geometry $\tilde{\Omega}_H$. Two thin layers of tissue are included to close the ventricular chambers at the level of the basal plane, representing $\tilde{\Omega}_C$. The geometrical surfaces are then labeled according to Fig. 2. Once the tetrahedral mesh is generated, the cardiac reference configuration $\Omega_H^0 \cup \Omega_C^0$ is computed by preprocessing the heart-caps domain $\tilde{\Omega}_H \cup \tilde{\Omega}_C$ as described in Section 2.6. Since the elements in the heart and caps are deformed during the computation of

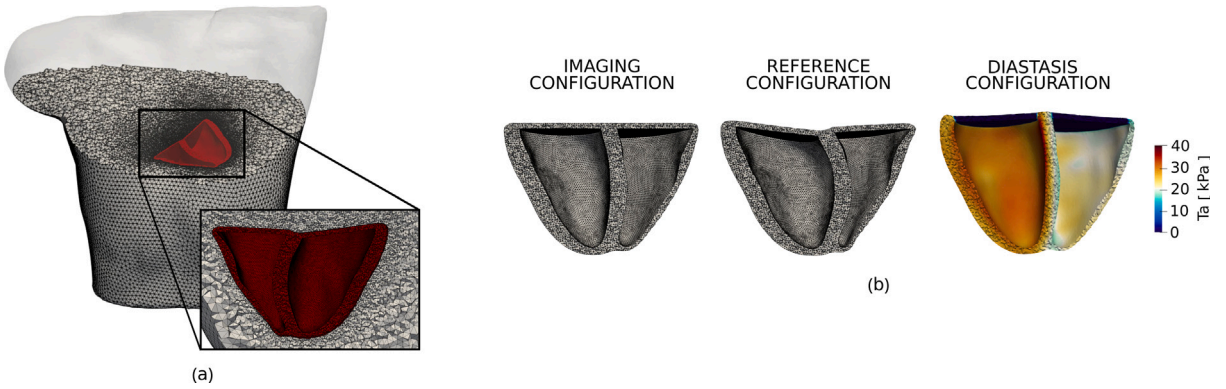

Fig. 4. (a) Volumetric geometries for the EMT model. (b) Cardiac imaging configuration, reference configuration Ω_H^0 and diastasis configuration computed from the EM simulation at the diastasis phase of the heart beat. The active tension T_a for the diastasis configuration is also displayed.

the cardiac reference domains, a final remeshing of the cardiac reference configuration is carried out to improve mesh quality in $\Omega_H^0 \cup \Omega_C^0$ (see Fig. 4).

The torso volumetric model is derived from the 3D RIUNET torso model [93], which is publicly available in the online repository of the Center for Integrative Biomedical Computing [94]. The organs, including blood pools, and the atria are removed. The ventricles are substituted with our cardiac reference configuration. The torso reference configuration Ω_T^0 is obtained by generating a tetrahedral mesh within the torso, conforming to $\Omega_H^0 \cup \Omega_C^0$ (referred to Fig. 4 for the torso reference configuration mesh). All the processing and meshing procedures are performed using the open-source softwares `vmtk` [73,95] and `Paraview` [96].

The cardiac mesh $\Omega_H^0 \cup \Omega_C^0$ is composed of 135K vertices and 715K elements, with an average edge length of 1.6 mm [61,62]. The torso mesh is comprised of an additional 406K vertices and 2.46M elements, with an average edge length of 5.4 mm.

Both the mechanical and torso simulations are set with the same time step $\Delta t = \Delta t^{\mathrm{T}} = 1$ ms, while $\Delta t^{\mathrm{EP}} = 0.05$ ms is chosen for the electrophysiological problem, i.e. $N_{\mathrm{EP}} = 20$ and $N_{\mathrm{T}} = 1$. The ionic model is initialized by conducting a 1000-cycle long single-cell simulation for the TTP06 model. Initial circulation variables are calibrated at the limit cycle through the procedure described in Section 2.6. Although five heartbeats are simulated, the results are presented only for on the last two heartbeats to reduce the effects of initialization.

In Section 4.2, the biventricular conduction system is simplified down to five focal spherical activation points, illustrated in Fig. 5(a) , along with a thin, fast conduction layer on the endocardia, following the approach in [33].

In Section 4.3, we induced sustained VT with a figure-of-eight pattern through an isthmus, bordered laterally by scars that act as conduction blocks, as shown in Fig. 5(b). Following [58,97], we applied an S1–S2–S3–S4 stimulation protocol consisting of four Gaussian stimuli located on the septum near the scar zone (see Fig. 5). The first stimulus S1 is applied at time t =0 s, the second one S2 at $t = 0.45$ s, the third one S3 at $t = 0.75$ s, and the fourth one S4 at $t = 1.02$ s.

The classical 12-leads ECG is computed by placing the nine electrodes in realistic locations on the surface of the torso domain, as depicted in Fig. 5. The same 9 position are used for all the simulations.

In both test cases, all four combinations of cardiac and torso configurations from Section 3.2 are simulated. The static cardiac configuration is represented by the volume occupied by the heart in the diastasis phase (150 ms into the heartbeat), corresponding to classical imaging configurations. However, the original volumetric configuration $\tilde{\Omega}_H$, which ideally represents the heart in the diastasis phase, is never exactly captured in the cardiac electromechanical simulation. Given the significant role of the cardiac shape in the analysis presented in this work, in order to maximize consistency, the cardiac diastasis configuration is extracted in terms of cardiac displacement $\mathbf{d}_H$ directly from the electromechanical simulation (refer to Fig. 4 for a visual comparison between the reference and diastasis configurations).

The presented numerical framework has been implemented in `life`$^{\mathrm{x}}$ [64,98], an in-house high-performance C++ finite element library, based on `deal.II` [99], specifically designed for cardiac applications. All numerical simulations were performed using the `iHeart` cluster, a Lenovo SR950 with 192-Core Intel Xeon Platinum 8160, operating at 2100 GHz, and equipped with 1.7TB RAM, located at MOX, Dipartimento di Matematica, Politecnico di Milano. A simulation involving 5 heart-beats is approximately 11 h long using 48 cores, with only around 6% dedicated to torso computation. Consequently, the overall cost of an EMT model aligns with that of the EM model [62].

4.2. Healthy scenario

Healthy conditions are achieved by using the model parameter setting reported in [61], specifically tailored for the biventricular geometry. The results presented in Fig. 6, which include quantitative measurements of cardiac mechanics and blood circulation, demonstrate our model capability to simulate realistic mechanical contraction. Moreover, our EMT model allows for the integration of mechanical and electrophysiological aspects, yielding clinically relevant outputs and measurements. The Wiggers diagram in

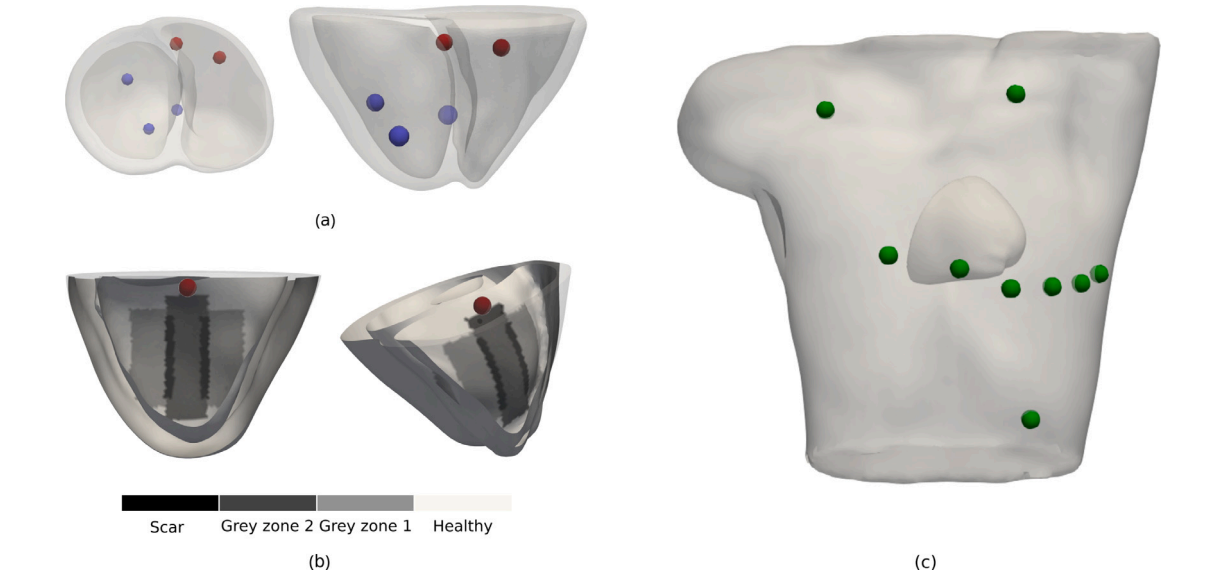

Fig. 5. (a) Location of the spherical impulses on the right (red spheres) and left (blue spheres) ventricles of the reference cardiac geometry $\Omega_H^0 \cup \Omega_C^0$ used to activate the heart for the test case in healthy conditions. (b) Cardiac reference geometry Ω_H^0 with the idealized distribution of scar (black), gray zones (gray), and healthy tissue (white) over the myocardium. The site of the activation point for the S1, S2, S3 and S4 pacing protocol is also depicted with a red sphere. (c) Position of the 9 electrodes (green spheres) to compute the 12-lead ECG. (For interpretation of the references to color in this figure legend, the reader is referred to the web version of this article.)

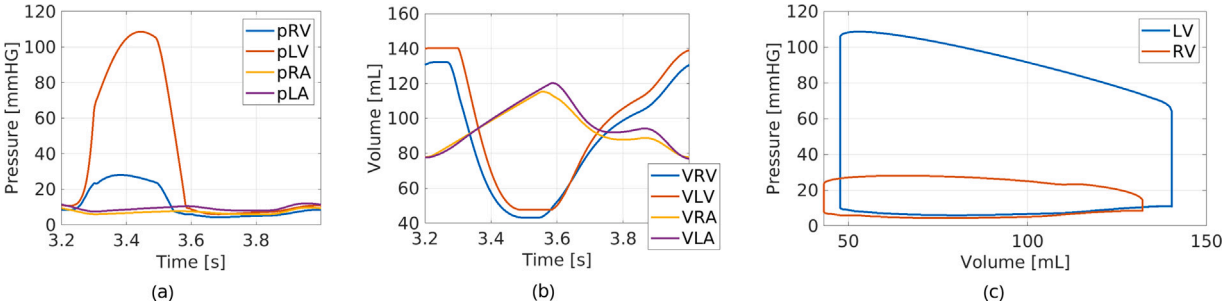

Fig. 6. Resulting traces of the circulatory system. (a) Pressures over time. (b) Volumes over time. (c) Pressure–volume loops in the ventricles.

Fig. 7 shows the alignment between systolic and diastolic phases, showcasing the heart contraction, ejection, and relaxation phases synchronized with the simulated ECG.

As illustrated in Fig. 8, we compare the transmembrane potential obtained on the deforming and static domain by projecting it on the static reference configuration. While the signal shape remains consistent, a noticeable reduction in the conduction velocities is observed when the MEFs are present, especially in the depolarization phase. This behavior can be explained by the alteration in conduction velocity when the EP properties remain constant, but the fibers elongate in accordance with the displacement of the heart. During depolarization, the heart static configuration is smaller than the configuration assumed due to cardiac mechanics. With the cardiac EP parameters predetermined, the elongation of fibers leads to a decrease in conduction velocity. Consequently, during the repolarization phase, when conduction velocity typically increases, the front of the signal on the moving heart lags behind that of the static configuration.

In Fig. 9, we depict a physiological QRS progression on the 12-lead ECG. Although the EP model lacks of heterogeneous apico-basal and transmural conduction velocities, which results in a non-physiological T wave, observed variations in the T wave due by myocardial contraction are independent from this heterogeneity, and can be therefore equally appreciated and investigated through this study.

Variations in transmembrane potential u and torso potential u_T are reflected in the corresponding ECG signals. In Fig. 9, the QRS complex and T wave obtained from four different simulation settings are presented. Although the overall shape remains consistent for each ECG, differences in waves shape and shift are noticeable in all leads.

Cardiac MEFs introduce a shift within the QRS wave in most leads, as observed when comparing signals obtained when the torso domain configuration is prescribed (see also Figs. 10 and 11). Although this shift corresponds to a prolonged QRS duration, the ECG waves remain aligned with the cardiac contraction, ejection, and relaxation phases observed in the EM simulations.

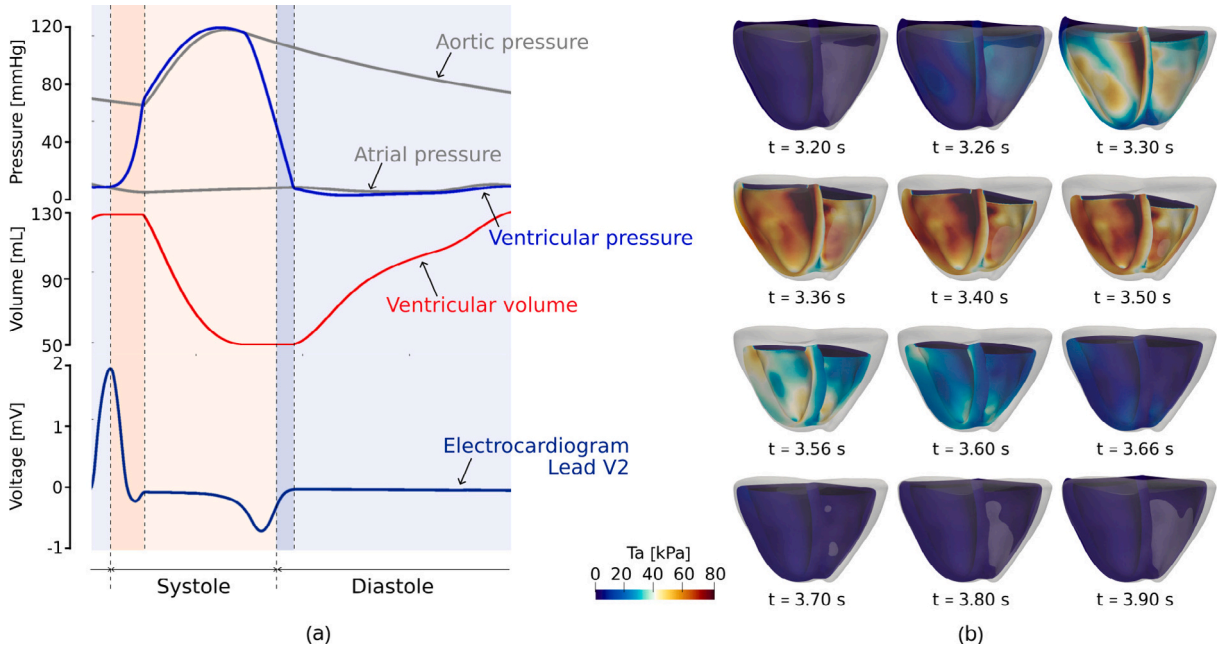

Fig. 7. (a) Wiggers diagram obtained by solving the EMT problem when both heart and torso are in moving configuration. Background color identifies the four phases of the cardiac cycle: isovolumic contraction (dark orange), ejection (light orange), isovolumic relaxation (dark blue), and the remaining part of the diastole (light blue). (b) Cardiac mechanical deformation and active tension T_a computed with the EMT model. (For interpretation of the references to color in this figure legend, the reader is referred to the web version of this article.)

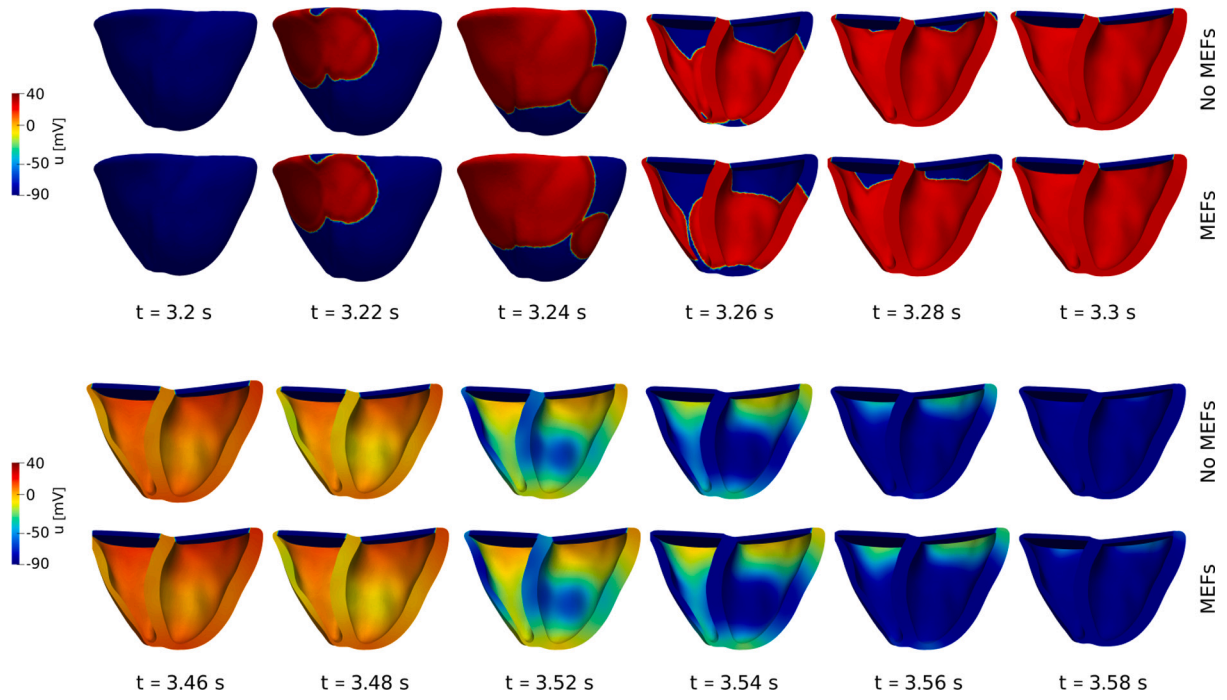

Fig. 8. Propagation of the transmembrane potential u on the cardiac reference domain Ω_H^0 when the electrophysiological problem is solved on a static configuration (no MEFs, rows 1 and 3), and when is solved on a moving configuration (with MEFs, rows 2 and 4).

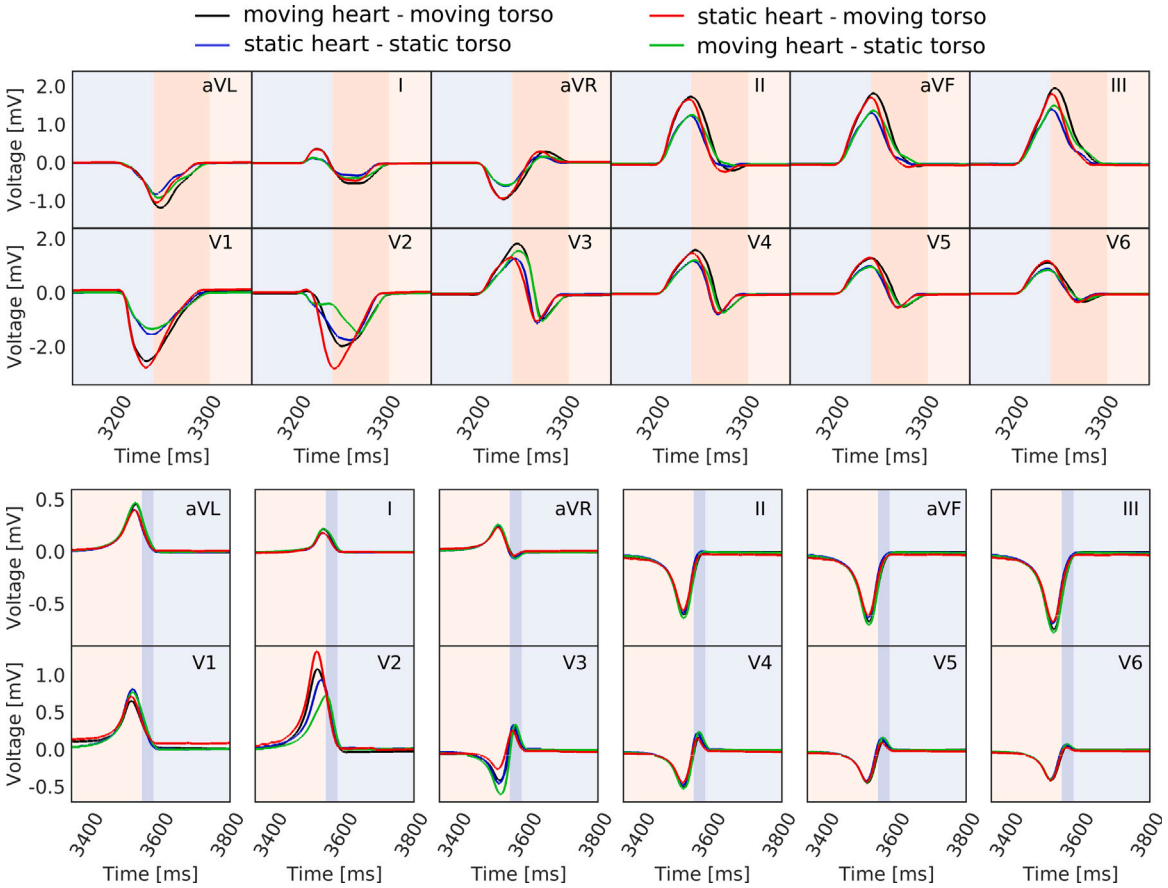

Fig. 9. QRS (top) and T wave (bottom) computed with the EMT model with the four configurations described in Section 3.2 and Table 1. Background color depicting four phases of the cardiac cycle: isovolumic contraction (dark orange), ejection (light orange), isovolumic relaxation (dark blue), and the remaining part of the diastole (light blue). (For interpretation of the references to color in this figure legend, the reader is referred to the web version of this article.)

Variations in torso potential, influenced by the deforming torso domain, result in changes in the amplitude of QRS waves. This effect is particularly prominent in limb leads II, III, aVR, and aVF. These leads are directly related to the left part of the torso, where the biventricular geometry is located, and consequently, the ECG and BSPMs are more influenced by the heart–torso interface deformation. Furthermore, substantial differences are observed in leads V_1, V_2 and V_3, which are closer to the cardiac domain and most susceptible to relative deformations (see also Figs. 12 and 13).

The T wave, corresponding to the repolarization phase, is generally less affected by the four different simulation settings. However, leads V_2 and V_3 still exhibit changes in amplitude corresponding to the maximal contraction of the heart.

Differences in signal propagation in the heart are also evident in the BSPMs depicted in Fig. 14. Starting from $t = 3.26\,\mathrm{s}$, variations in BSPMs become significant when the torso configuration is prescribed, with fluctuations based on different configurations of the cardiac domain (as in Table 1, this is observed by looking at the group of four BSPMs by columns). However, variations in BSPMs are not solely attributed to the cardiac MEFs. Different outcomes emerge when deforming the torso domain according to the cardiac displacement, instead of prescribing a static torso domain, as depicted in Fig. 14 (as in Table 1, this is observed by looking at the group of four BSPMs by rows).

To quantify differences in shape of two simulated ECG signals $\phi_1(i)$ and $\phi_2(i)$, $i = 1, \dots, N_T$, we use the following linear correlation coefficient (CC)

$$\mathrm{CC} = \frac{1}{s_1 s_2} \sum_{i=1}^{N_T} \left[\phi_1(i) - \overline{\phi_1}\right] \left[\phi_2(i) - \overline{\phi_2}\right], \tag{6}$$

for each lead and its average across all leads. Here, s_1 and s_2 are the standard deviation of ϕ_1 and ϕ_2, respectively, while $\overline{\phi_1}$ and $\overline{\phi_2}$ are the corresponding arithmetic average values. The CCs between signals, obtained by reading Table 1 by columns and rows, are reported in Tables 2 and 3. This highlights a shift in the ECG wave, with the highest correlation coefficients corresponding to the heart–torso configuration with a prescribed torso.

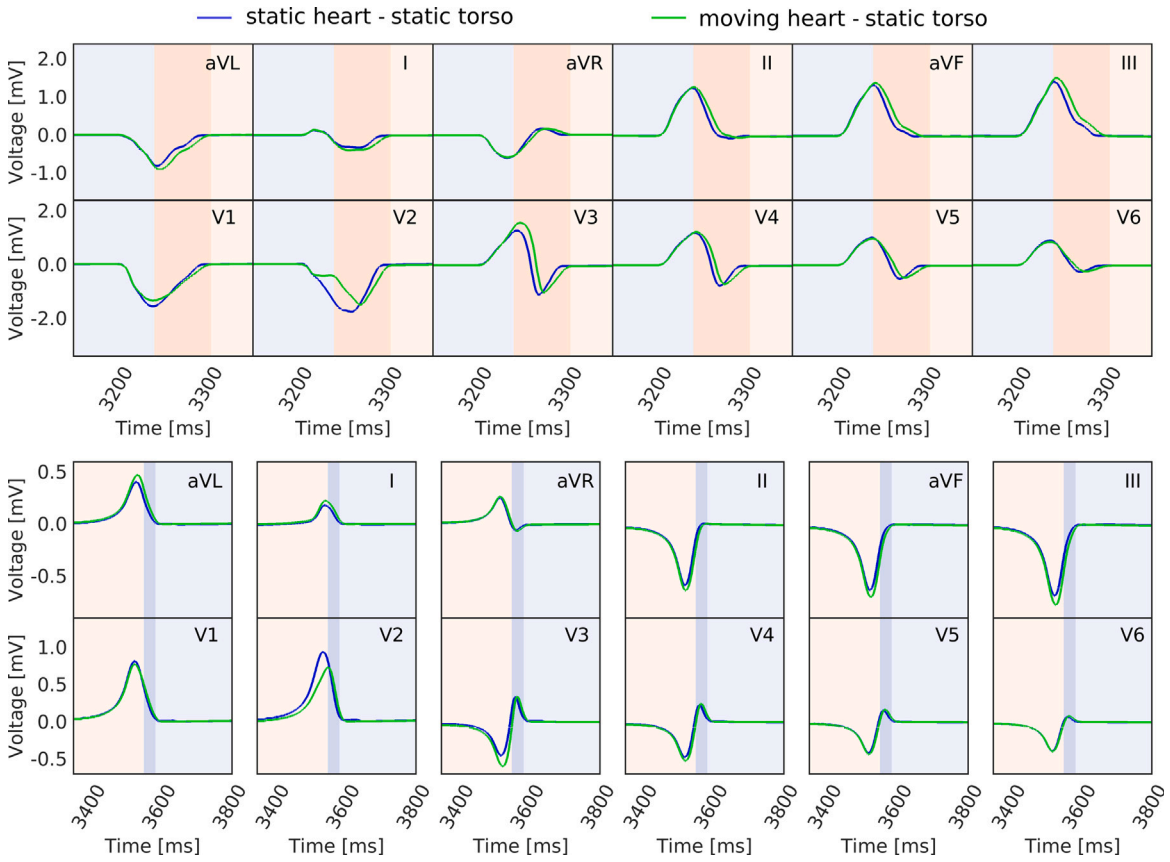

Fig. 10. QRS (top) and T wave (bottom) computed with the EMT model when the torso is considered as a static domain, and the heart is either static or dynamic. Background color identifies four phases of the cardiac cycle: isovolumic contraction (dark orange), ejection (light orange), isovolumic relaxation (dark blue), and the remaining part of the diastole (light blue). (For interpretation of the references to color in this figure legend, the reader is referred to the web version of this article.)

4.3. Pathological scenario

Sustained VT is simulated in the biventricular geometry through an idealized septal ischemia. The VT is induced using an S1-S2-S3-S4 stimulation protocol, where different stimuli are applied at $t = 0\,\mathrm{s}$, $t = 0.45\,\mathrm{s}$, $t = 0.75\,\mathrm{s}$ and $t = 1.02\,\mathrm{s}$ on the top part of the isthmus [58]. To the best of our knowledge, this is the first time in which a VT is simulated using a fully-coupled 3D–0D EMT model in a biventricular geometry. In Fig. 15, we display different snapshots of displacement magnitude by considering the heart in the dynamic configuration. However, as we are primarily focused on observing electrophysiological bio-markers, we will limit our analysis to ECG and BSPMs, while employing the EMT model with different heart–torso configurations.

In the EM simulation, we observe the formation and sustainment of a polymorphic VT. On the other hand, running an EMT simulation with a moving cardiac domain induces a stable monomorphic VT. This is evident in both the transmembrane potential propagation on the cardiac domain, as shown in Fig. 16, and the ECG traces presented in Figs. 18 and 19.

We compare BSPMs and ECGs obtained by solving the EMT model with the heart in a dynamic domain, and the torso in either static or dynamic configuration.

BSPMs for the static and moving configurations of the heart are illustrated in Fig. 17. Differences in signal magnitude are present, while the overall signal distribution remains consistent across the entire torso surface.

The ECG traces, depicted in Fig. 20, showcase variations in the amplitude of both the QRS complex and T-wave in all limb leads and leads V_1, V_2, V_3, with other precordial leads remaining largely unchanged. Alteration in T-wave shape are mostly noticeable in the limb leads, particularly in lead I, where T-wave inversion is consistently observed throughout all heartbeats.

The CCs over the entire set of leads are reported in Table 4, confirming the substantial impact of torso domain pseudo-deformation on the ECG, especially in leads I and II. The average CC is also generally smaller than the corresponding values obtained in healthy simulations, showing a greater shape variation in pathological simulations rather than healthy ones.

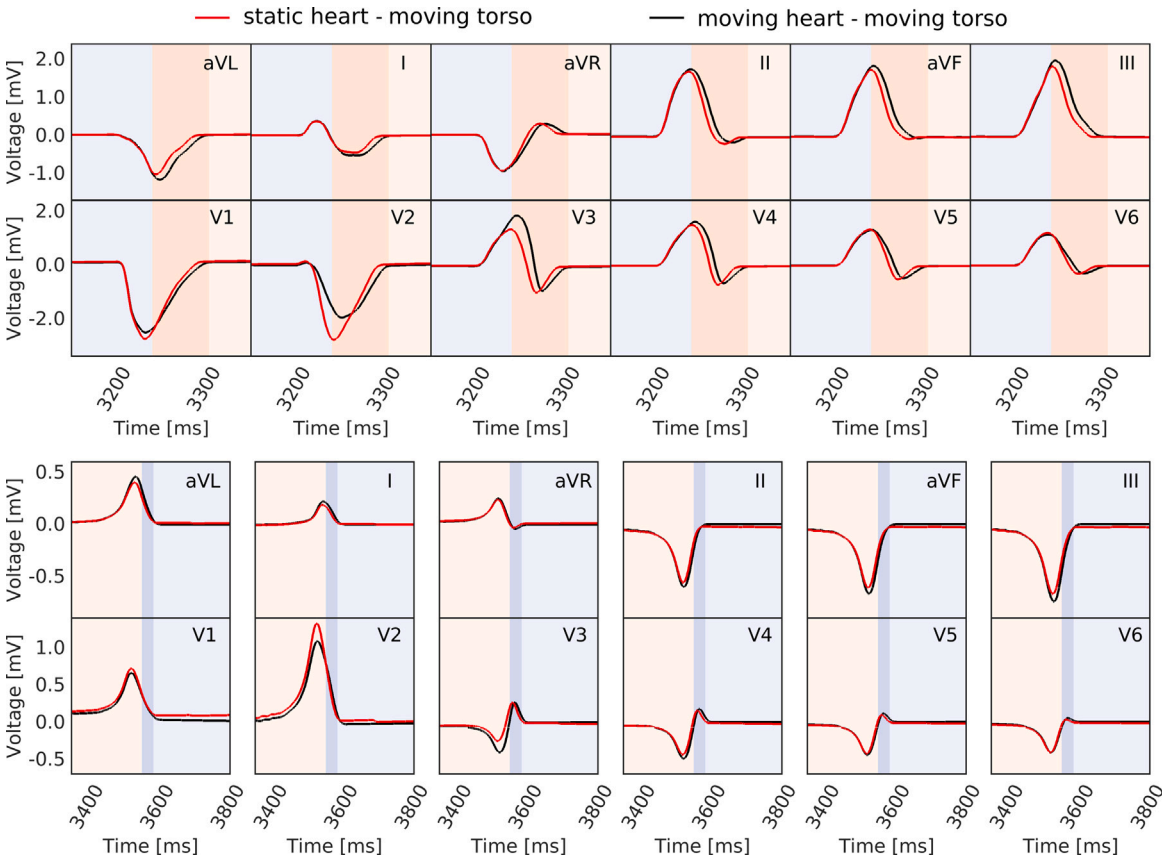

Fig. 11. QRS (top) and T wave (bottom) computed with the EMT model when the torso is considered as a moving domain, and the heart is either static or dynamic. Background color identifies the four phases of the cardiac cycle: isovolumic contraction (dark orange), ejection (light orange), isovolumic relaxation (dark blue), and the remaining part of the diastole (light blue). (For interpretation of the references to color in this figure legend, the reader is referred to the web version of this article.)

Table 2
QRS correlation coefficients (CC) in the standard 12 leads of a healthy patient between different heart–torso configurations. The first two rows correspond to a column-wise interpretation of Table 1, while rows 3 and 4 represent a row-wise reading of Table 1. Row 5 reports the comparison between the classical EP-torso configuration and the new coupling presented in our work. The average CC across all leads is included in the last column. For leads with largest ECG shape variations, we highlighted in red the configuration with smallest CC (highest variation) and in green the configuration with largest CC (smaller variation).

	CC												
Heart–torso vs heart–torso	aVL	I	aVR	II	aVF	III	V_1	V_2	V_3	V_4	V_5	V_6	mean
Static–static vs moving–static	0.9763	0.9763	0.9847	0.9811	0.9786	0.9770	0.9911	0.8550	0.8765	0.9425	0.9677	0.9864	0.9578
Moving–moving vs static–moving	0.9723	0.9779	0.9791	0.9746	0.9723	0.9711	0.9939	0.9209	0.8216	0.9316	0.9616	0.9817	0.9549
Moving–moving vs moving–static	0.9942	0.9624	0.9981	0.9973	0.9978	0.9979	0.9758	0.8682	0.9926	0.9907	0.9924	0.9988	0.9805
Static–static vs static–moving	0.9946	0.9629	0.9950	0.9960	0.9974	0.9982	0.9703	0.9360	0.9668	0.9937	0.9958	0.9996	0.9839
Static–static vs moving–moving	0.9611	0.9512	0.9867	0.9856	0.9818	0.9756	0.9858	0.9744	0.8892	0.9117	0.9427	0.9796	0.9604

Table 3
T wave correlation coefficients (CC) in the standard 12 leads of a healthy case between different heart–torso configurations. The first two rows correspond to a column-wise interpretation of Table 1, while rows 3 and 4 represent a row-wise reading of Table 1. Row 5 reports the comparison between the classical EP-torso configuration and the new coupling presented in our work. The average CC across all leads is included in the last column. For leads with largest ECG shape variations, we highlighted in red the configuration with smallest CC (highest variation) and in green the configuration with largest CC (smaller variation).

	CC												
Heart–torso vs heart–torso	aVL	I	aVR	II	aVF	III	V_1	V_2	V_3	V_4	V_5	V_6	mean
Static–static vs moving–static	0.9935	0.9939	0.9952	0.9943	0.9939	0.9936	0.9968	0.9572	0.9517	0.9839	0.9912	0.9966	0.9868
Moving–moving vs static–moving	0.9928	0.9921	0.9909	0.9919	0.9923	0.9926	0.9886	0.9905	0.8598	0.9772	0.9894	0.9954	0.9795
Moving–moving vs moving–static	0.9985	0.9982	0.9955	0.9968	0.9975	0.9979	0.9808	0.9198	0.9853	0.9959	0.9916	0.9941	0.9877
Static–static vs static–moving	0.9993	0.9973	0.9991	0.9993	0.9993	0.9993	0.9934	0.9614	0.9263	0.9988	0.9952	0.9966	0.9888
Static–static vs moving–moving	0.9905	0.9958	0.9897	0.9878	0.9881	0.9889	0.9842	0.9834	0.9790	0.9764	0.9767	0.9872	0.9857

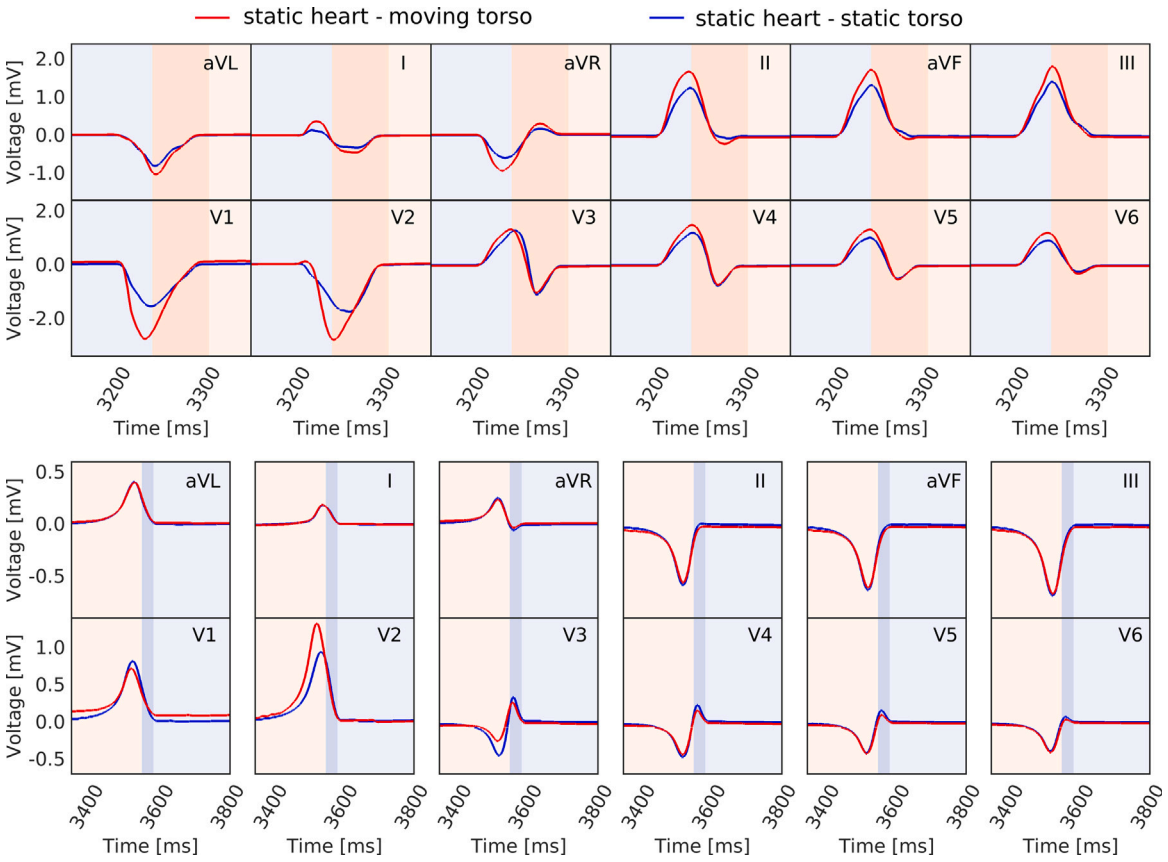

Fig. 12. QRS (top) and T wave (bottom) computed with the EMT model when the heart is considered as a static domain, and the torso is either static or dynamic. Background color identifies the four phases of the cardiac cycle: isovolumic contraction (dark orange), ejection (light orange), isovolumic relaxation (dark blue), and the remaining part of the diastole (light blue). (For interpretation of the references to color in this figure legend, the reader is referred to the web version of this article.)

Table 4
Correlation coefficients (CC) between the standard 12 leads of a pathological case, computed when the heart is considered in a moving domain (first row), and with the classical EP-torso configuration vs the new coupling presented in our work (second row). The average CC across all leads is included in the last column. When comparing the moving heart — static torso and moving heart — moving torso configurations, largest variations are highlighted with red color.

	CC												
Heart–torso vs heart–torso	aVL	I	aVR	II	aVF	III	V_1	V_2	V_3	V_4	V_5	V_6	mean
Moving–moving vs static–moving	0.7763	0.9180	0.9676	0.9658	0.9506	0.9076	0.9807	0.9840	0.9915	0.9985	0.9986	0.9986	0.9531
Static–static vs moving–moving	0.1880	-0.4747	-0.3101	-0.1750	-0.0669	0.0652	-0.1816	0.0249	0.0908	0.1046	0.0430	0.0241	-0.0556

5. Discussion

In the simulation of cardiac healthy conditions, our model demonstrates its ability to accurately represent physiological scenarios in agreement with reference values from the medical literature of pressure and volume loops, ECGs and BSPMs. The interplay of mechanical deformation on the ECG and BSPMs is highlighted, revealing a direct link between cardiac MEFs and variations in ECG and BSPM signals. Differently than in [57], our model features shifts and prolongations of QRS waves across all leads during the contraction and ejection phases. Additionally, amplitude variations are observed in ECG signals, particularly in the limb leads associated with the left torso and precordial leads V_1, V_2, and V_3, primarily attributed to torso domain deformation. T-wave variations are predominantly registered in lead V_2, in line with [57], emphasizing changes in wave amplitude.

Regarding the pathological conditions, a VT is simulated by defining a sustained figure-of-eight reentry with an idealized isthmus located at the (bi)ventricular septum. Moreover, we highlight the impact of the cardiac MEFs on the propagation of the electrical signal. Indeed, MEFs may transform the nature of the simulated VT from polymorphic to monomorphic, therefore altering ECG and BSPM patterns. While in this case cardiac MEFs have a prominent role in changing the EP signal, effect of the torso domain deformation has also been observed. Specifically, changes in amplitude and shape of the ECGs are shown, with major variations in lead I, where inverted polarity in the T wave is achieved.

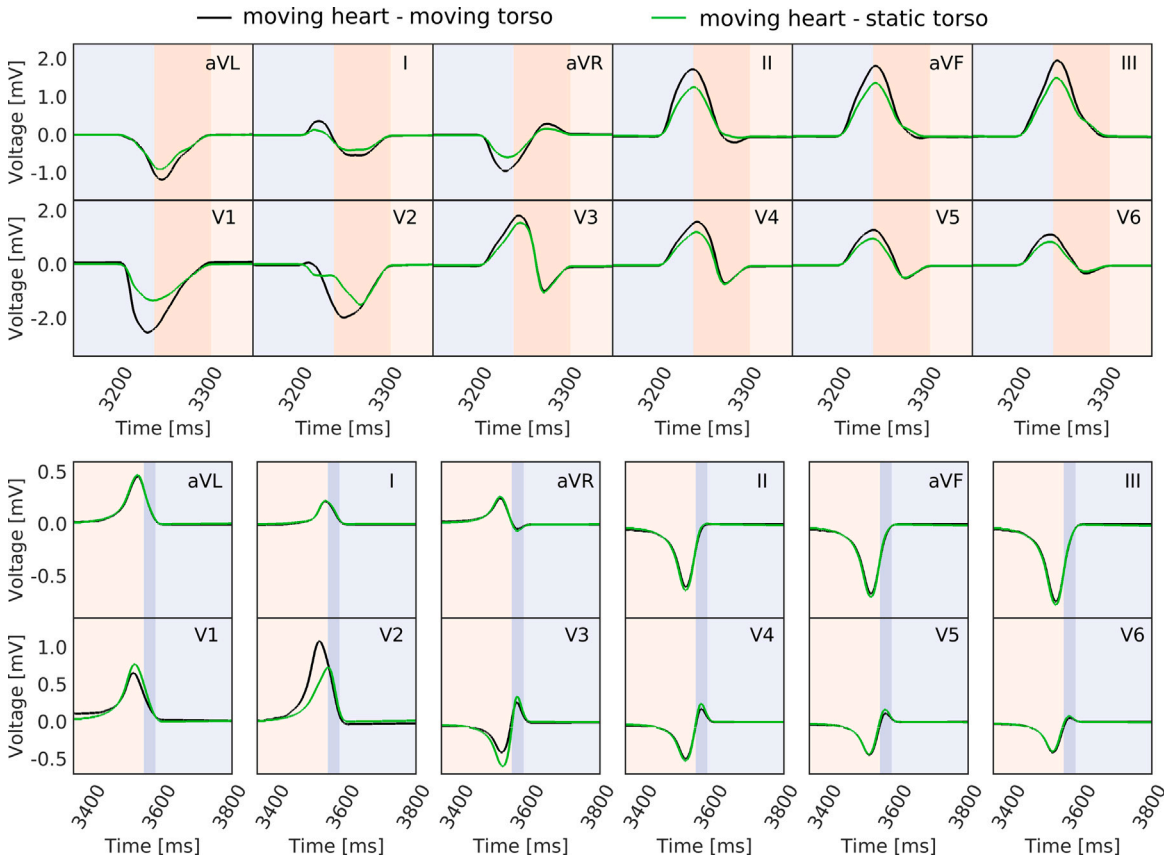

Fig. 13. QRS (top) and T wave (bottom) computed with the EMT model when the heart is considered as a moving domain, and the torso is either static or dynamic. Background color identifies the four phases of the cardiac cycle: isovolumic contraction (dark orange), ejection (light orange), isovolumic relaxation (dark blue), and the remaining part of the diastole (light blue). (For interpretation of the references to color in this figure legend, the reader is referred to the web version of this article.)

Compare to the more recent EM computational model presented in [57], our methodology still ensures complete equivalence in terms of physical modeling, as we address the same underlying mathematical problem, but features some differences in terms of computational methods and capacity of simulating pathological scenario. Specifically, in [57] the authors constructed a halo around the four-chamber heart within the torso geometry. For each new heart configuration defined by the solution of an electromechanical model [100], a new mesh on the halo was created to account for the altered heart shape. Subsequently, the BEM was solved within the halo-torso geometry to calculate the ECGs and the BSPMs. This modeling approach, therefore, necessitated a remeshing stage for each time instance of EP output computation. Moreover, due to the use of BEM, it lacked the capability to represent anisotropic conduction properties in the extracellular space, which became significant in pathological scenarios. Conversely, our approach avoids the necessity for remeshing, and allows for ECGs and BSPMs computation even for pathological conditions.

Furthermore, in the present work the influence of MEFs on EM outcomes results to be important and more pronounced than in the test cases presented in [59,63]. It therefore remains unclear how the chosen MEFs and cardiac geometry can impact the simulation outputs. Nevertheless, our findings indicate that both MEFs and cardiac geometry can lead to distinct outcomes, particularly in the propagation of EP signals. Further insights could be gained by testing the proposed EMT model on a cohort of four-chamber hearts, similar to the one presented in [101]. Moreover, numerous studies have demonstrated that the position, dimensions, and shape of the heart [29,30], along with the presence and configuration of organs within the torso [102,103], can impact the shape and amplitude of ECGs. This further highlight the need to expand the range of cardiac and torso domains considered in this analysis.

The first limitation of our approach resides in the representation of heterogeneous cardiac conduction properties, which influence T-wave shape and polarity, as well as a realistic representation of the Purkinje network. Moreover, our electromechanical coupling lacks the representation of the stretch activated channels. These features would improve the biophysical accuracy of the mathematical model and further elucidate the role of MEFs in EMT simulations.

Another limitation of our study is the use of a relatively coarse mesh size in the cardiac domain for solving the EP model. However, the conduction coefficients are adjusted based on this mesh size, and second-order finite element are employed to ensure physiological conduction velocities, following the approach described by [68]. Furthermore, this mesh resolution, combined with quadratic finite element, has been previously successfully utilized to model the physiological cardiac function in sinus

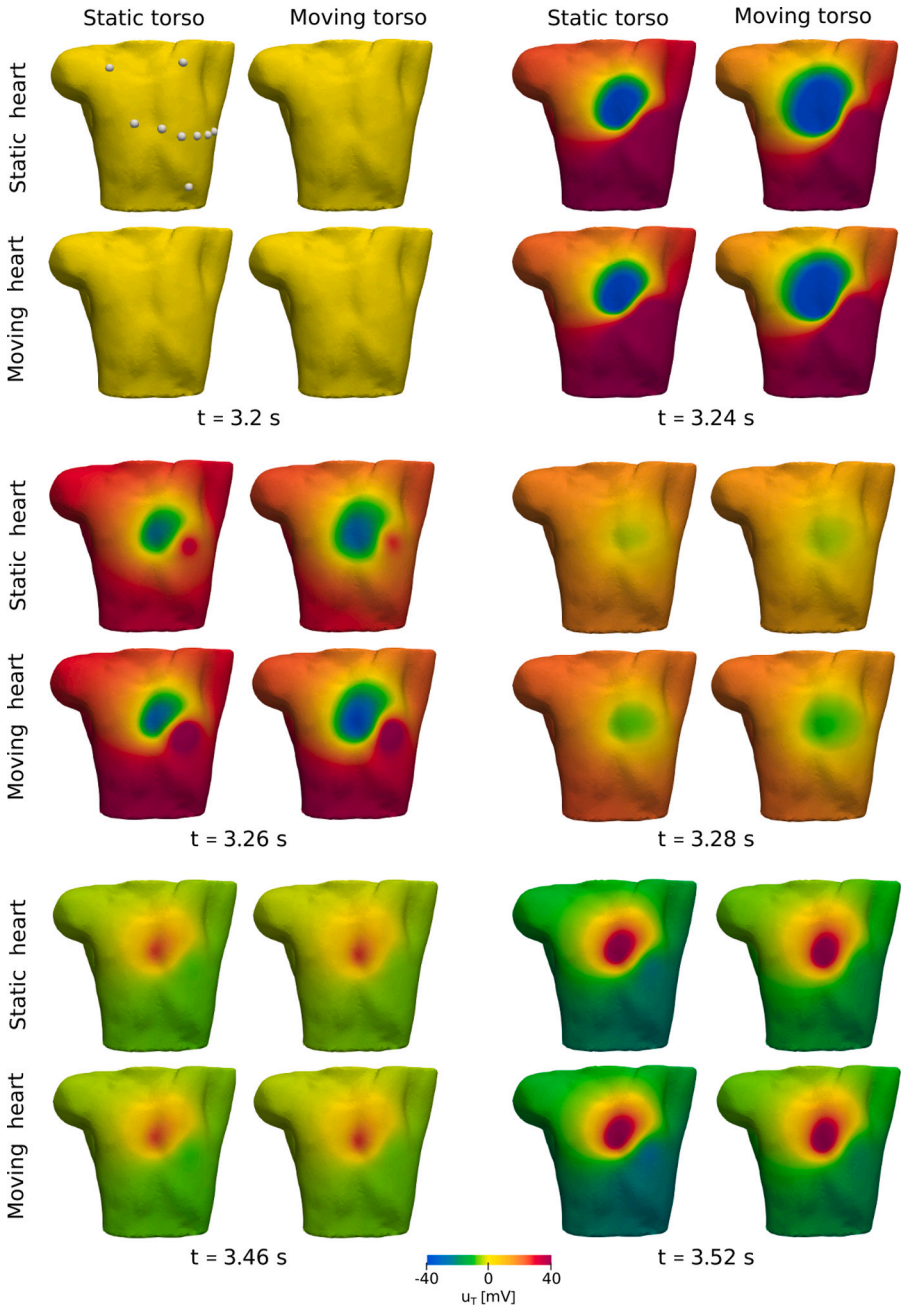

Fig. 14. BSPMs on selected time instants for all four combinations of cardiac and torso configurations reported in Table 1. The electrodes locations are also reported.

rhythm [61,62], as well as under pathological conditions [58,59,65]. We underline that the primary aim of this work is to compare ECGs and BSPMs across different coupling of cardiac electromechanical and torso diffusion models, and to explore how cardiac displacement affects electrophysiological outputs. Since we have consistently used the same mesh size, numerical methods, and model parameters across all simulations, we believe that our results are not affected by the potential limitations imposed by the selected mesh size.

A potential extension of our model could involve a more physiologically accurate representation of the torso. This enhancement would include the addition of conduction homogeneities in correspondence to lungs, bones, fat, and skin. Additionally, it has been shown that the respiratory motion plays an important role in determining the shape of both the heart and the torso [104–106],

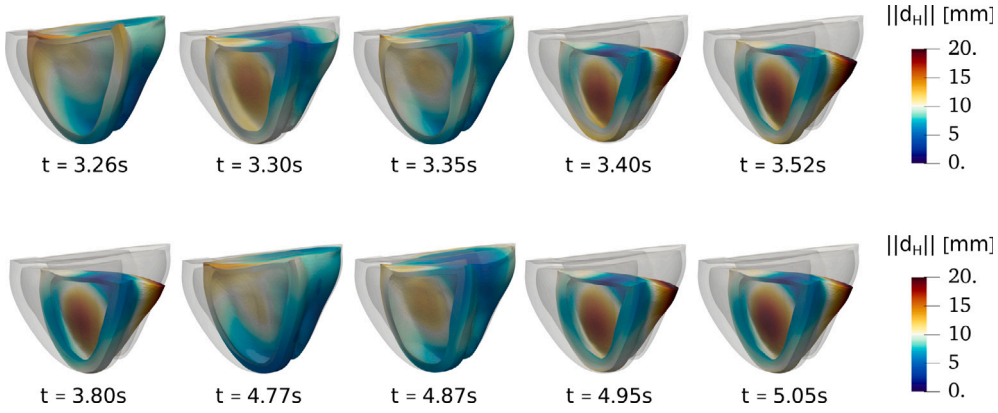

Fig. 15. Displacement $\mathbf{d}_H$ simulated with the EMT model and MEFs on the heart.

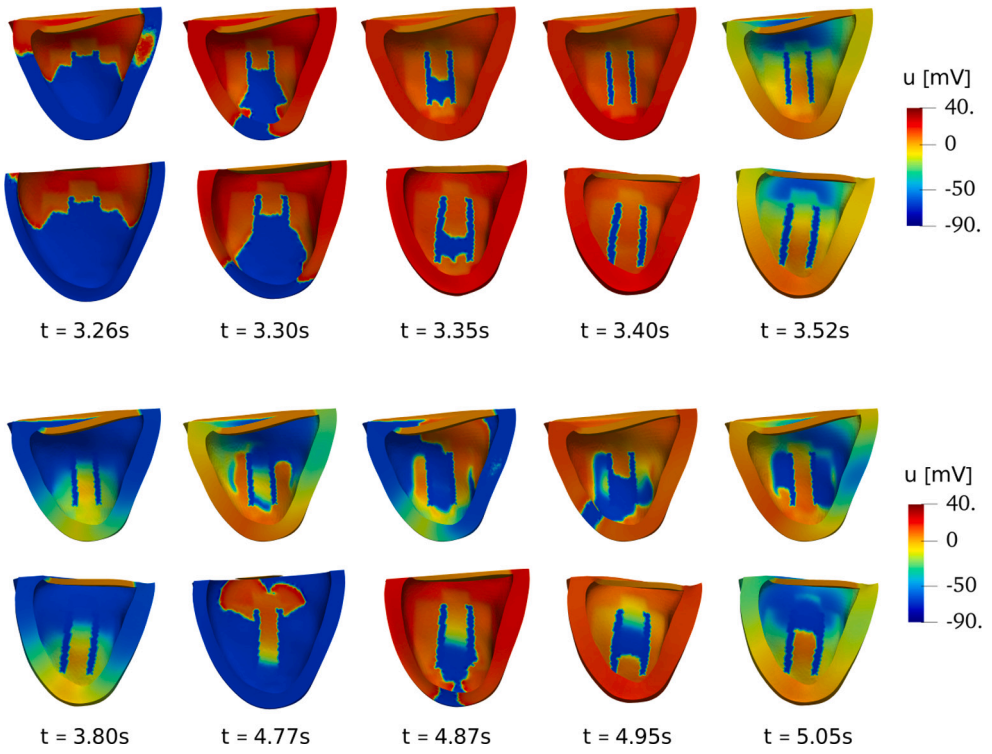

Fig. 16. Propagation of the transmembrane potential u on the heart Ω_H when the electrophysiological problem is solved on a static configuration (no MEFs, rows 1 and 3), and when is solved on a moving configuration (with MEFs, rows 2 and 4). When MEFs are activated, the cardiac geometry is warped by vector to show the deformation caused by the electro-mechanical interaction.

thus furthermore changing the position of the cardiac electrical sources and their distance from the electrode . Therefore, another separate improvement lay in the implementation of the torso and cardiac deformation resulting from the respiratory motion.

6. Conclusions

In this study, we introduced an EMT model by unidirectionally coupling an EM model of the heart with a passive conductive model of the torso. This mathematical model dynamically defines the torso domain deformation resulting from myocardial displacement. The flexible segregated–intergrid–staggered numerical framework employed allows for the arbitrary and independent selection of the cardiac displacement used to solve both the Monodomain model and to modify the torso domain, which is equivalent to employ static or dynamic cardiac and torso domain configurations. This allows to explore the impact of myocardial deformation

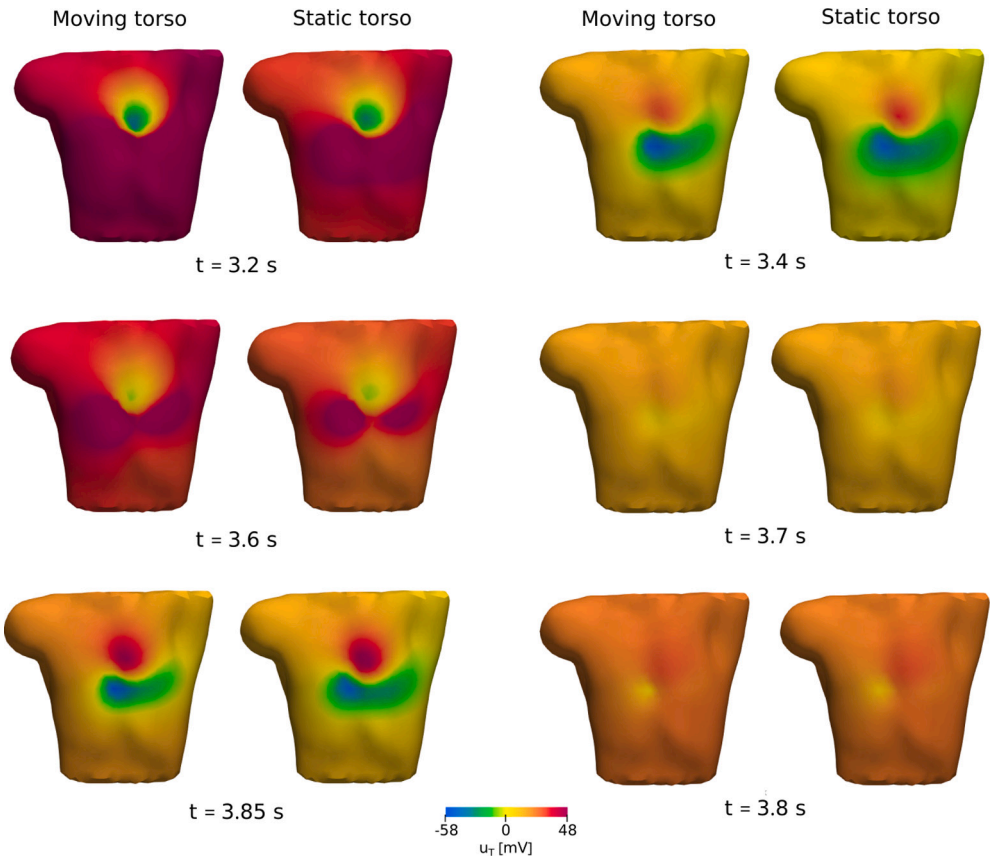

Fig. 17. BSPMs on selected time instants computed with a prescribed cardiac moving configuration according to the second row of Table 1.

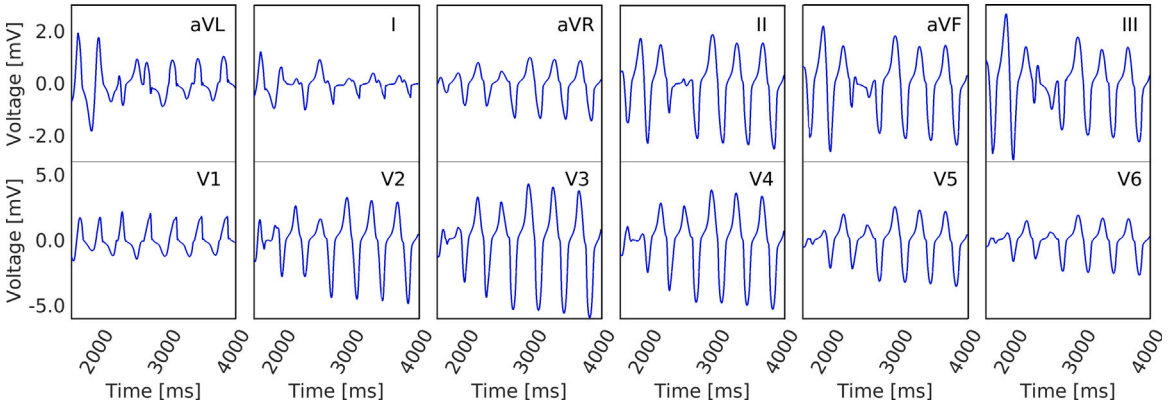

Fig. 18. 12-lead ECG computed considering both cardiac and torso domain in static configurations. The ECGs represent a polymorphic VT .

on EP propagation and, consequently, on the ECG and BSPMs, as well as investigate the influence of shifting the heart–torso surface, and thereby the torso domain, on EP outputs.

The model is tested under both healthy and pathological scenarios, the latter involving cardiac arrhythmias, specifically VT. To ensure fairness in our comparison, as static configuration, the displacement of the cardiac geometry in the end-diastolic phase is extracted from the EM simulation and imposed to the Monodomain and torso lifting problem. Overall, based on the results obtained from our model, we concluded that the influence of cardiac contraction on EP outputs should not be underestimated, particularly when simulating pathological conditions.

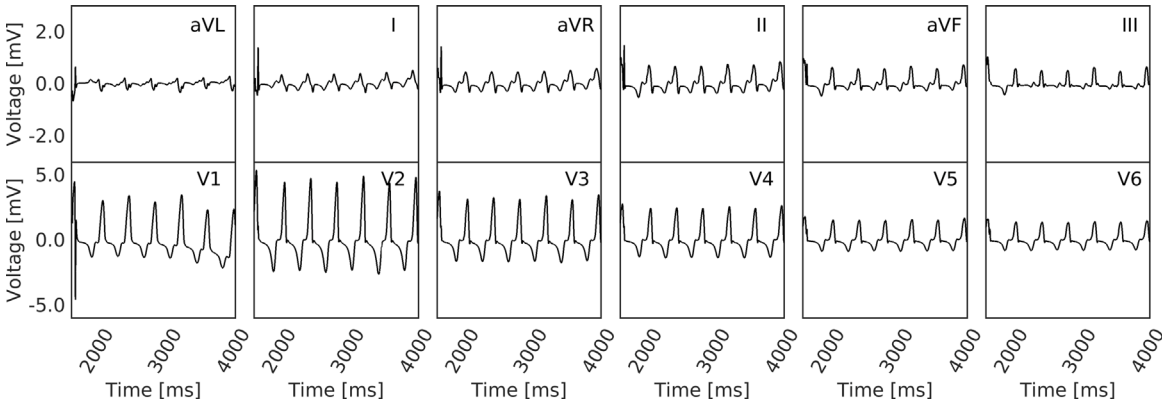

Fig. 19. 12-lead ECG computed considering both cardiac and torso domain in dynamic configurations. The ECGs represent a monomorphic VT .

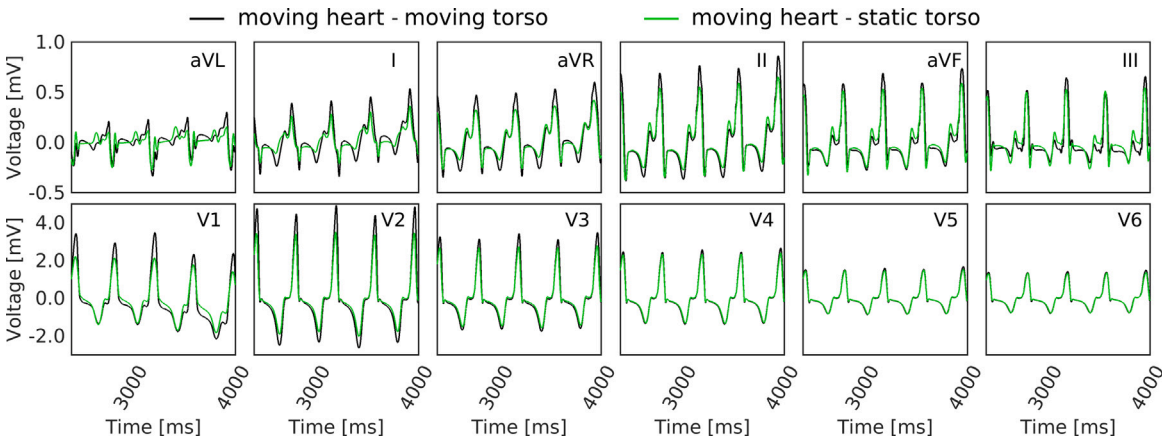

Fig. 20. Comparison of 12 lead ECGs when the EMT model is solved in a cardiac moving configurations. The ECGs represent a monomorphic VT .

CRediT authorship contribution statement

Elena Zappon: Writing – review & editing, Writing – original draft, Validation, Software, Methodology, Formal analysis, Conceptualization. **Matteo Salvador:** Writing – review & editing, Validation, Software, Conceptualization. **Roberto Piersanti:** Writing – review & editing, Validation, Conceptualization. **Francesco Regazzoni:** Writing – review & editing, Software, Methodology, Conceptualization. **Luca Dede':** Writing – review & editing, Supervision. **Alfio Quarteroni:** Writing – review & editing, Supervision, Funding acquisition.

Declaration of competing interest

The authors declare the following financial interests/personal relationships which may be considered as potential competing interests: R. Piersanti F. Regazzonii L. Dede' report financial support was provided by Ministry of University and Research Italy. E. Zappon R. Piersanti F. Regazzoni L. Dede' report travel was provided by National Group for Scientific Computing, Italy. If there are other authors, they declare that they have no known competing financial interests or personal relationships that could have appeared to influence the work reported in this paper.

Data availability

No data was used for the research described in the article.

Acknowledgments

The present research is part of the activities of "Dipartimento di Eccellenza 2023–2027", MUR, Italy, Dipartimento di Matematica, Politecnico di Milano. R. Piersanti and L. Dede' have received support from the project PRIN2022, MUR, Italy, 2023–2025,

202232A8AN "Computational modeling of the heart: from efficient numerical solvers to cardiac digital twins". F. Regazzoni has received support from the project PRIN2022, MUR, Italy, 2023–2025, P2022N5ZNP "SIDDMs: shape-informed data-driven models for parametrized PDEs, with application to computational cardiology". R. Piersanti has received support from the INdAM GNCS project CUP E53C23001670001. The authors acknowledge their membership to INdAM GNCS — Gruppo Nazionale per il Calcolo Scientifico (National Group for Scientific Computing, Italy). This project has been partially supported by the INdAM-GNCS Project CUP E53C22001930001.

Appendix. Cardiac electro-mechanical model

In this Appendix we report the mathematical models employed to define cardiac electromechanics and cardiovascular hemodynamics. These models are also briefly described and accounted for in Section 2. Finally, the 12-lead ECG system is described in the last section.

A.1. Electrophysiological model

The cardiac transmembrane potential u is computed by solving the Monodomain model endowed with gradient deformation tensors to account for the mechanical displacement on the potential propagation. Specifically, the formulation of the Monodomain model reads:

$$\begin{cases} \chi\left[C_{\mathrm{m}}\dfrac{\partial u}{\partial t}+I_{ion}(u,\mathbf{w},\mathbf{c})\right]-\nabla\cdot(J_H\mathbf{F}_H^{-1}\mathbf{D}_m\mathbf{F}_H^{-T}\nabla u) & \\ \qquad =J_H\chi_{\mathrm{m}}I_{app}(t) & \text{in } \{\Omega_H^0\cup\Omega_C^0\}\times(0,T], \quad (A.1a)\\ \dfrac{\partial \mathbf{w}}{\partial t}-\boldsymbol{H}(u,\mathbf{w})=\mathbf{0} & \text{in } \{\Omega_H^0\cup\Omega_C^0\}\times(0,T], \quad (A.1b)\\ \dfrac{d\mathbf{z}}{dt}=\mathbf{G}(u,\mathbf{w},\mathbf{z}) & \text{in } \{\Omega_H^0\cup\Omega_C^0\}\times(0,T], \quad (A.1c)\\ (J_H\mathbf{F}_H^{-1}\mathbf{D}_m\mathbf{F}_H^{-T}\nabla u)\cdot\mathbf{n}_H=0 & \text{on } \partial\{\Omega_H^0\cup\Omega_C^0\}\times(0,T], \quad (A.1d)\\ u=u_{m,0},\ \mathbf{w}=\mathbf{w}_0,\ \mathbf{z}=\mathbf{z}_0 & \text{in } \{\Omega_H^0\cup\Omega_C^0\}\times\{t=0\}. \quad (A.1e)\end{cases}$$

where C_m is the capacitance per unit area, and χ is the surface-to-volume ratio of the membrane. Here I_{app} is a function representing the activation sites used as pacing protocol (referred to Section 4), and $\mathbf{D}_m$ is the conductivity tensor, computed as:

$$\boldsymbol{D}_m=\mu\sigma_\ell^m\frac{\mathbf{F}_H\mathbf{f}_0\otimes\mathbf{F}_H\mathbf{f}_0}{\|\mathbf{F}_H\mathbf{f}_0\|^2}+\mu\sigma_t^m\frac{\mathbf{F}_H\mathbf{s}_0\otimes\mathbf{F}_H\mathbf{s}_0}{\|\mathbf{F}_H\mathbf{s}_0\|^2}+\mu\sigma_n^m\frac{\mathbf{F}_H\mathbf{n}_0\otimes\mathbf{F}_H\mathbf{n}_0}{\|\mathbf{F}_H\mathbf{n}_0\|^2},$$

The conduction coefficients $\sigma^m_{\ell,t,n}$ are strictly related to the extracellular and intracellular conduction coefficients by means of the following formula:

$$\sigma^m_{\ell,t,n}=\frac{\sigma^i_{\ell,t,n}\sigma^e_{\ell,t,n}}{\sigma^i_{\ell,t,n}+\sigma^e_{\ell,t,n}}.$$

Eqs. (A.1b)–(A.1c) stand for the ionic model.

A.2. Cardiomyocyte active contraction

The cardiomyocyte active contraction is modeled with either the RDQ18 and RDQ20 models, which have the following structure:

$$\begin{cases}\dfrac{\partial\mathbf{s}}{\partial t}=\boldsymbol{K}(\mathbf{s},[\mathrm{Ca}^{2+}]_{\mathrm{i}},SL,\dfrac{dSL}{dt}) & \text{in } \{\Omega_H^0\cup\Omega_C^0\}\times(0,T], \quad (A.2a)\\ \mathbf{s}=\mathbf{s}_0 & \text{on } \{\Omega_H^0\cup\Omega_C^0\}\times\{t=0\}, \quad (A.2b)\end{cases}$$

where the unknown is the vector $\mathbf{s}$ of state variables, $\mathbf{K}$ a suitable function (see [107]), and SL is obtained from the mechanical model as:

$$SL=SL_0\sqrt{\mathcal{I}_{4f}(\mathbf{d}_H)}.$$

The variable SL_0 is the sarcomeres length at rest, while $\mathcal{I}_{4f}=\mathbf{F}_H\mathbf{f}_0\cdot\mathbf{F}_H\mathbf{f}_0$ is a measure of the tissue stretch along the fibers direction.

The active tension T_a is computed as:

$$T_a(\mathbf{s})=T_a^{\max}G(\mathbf{s},P)\left[\hat{\xi}+C_{LRV}(1-\hat{\xi})\right],$$

where P is the permissivity, that is the fraction of contractile units being in the force-generation state, $T_a^{\max}$ is the total tension generated (obtained when $P=1$), $G(\mathbf{s})$ is a linear function related to the permissivity [72], $\hat{\xi}\in[0,1]$ is the normalized intra-ventricular distance, and $C_{LRV}\in(0,1]$ is the left–right ventricular contractility ratio.

A.3. Cardiac active and passive contraction

The large deformation of the cardiac tissue is described through the finite elasticity theory. The displacement $\mathbf{d}_H$ is obtained by solving the momentum conservation equation endowed with proper boundary conditions and a formulation for of the Piola–Kirchhoff stress tensor $\mathbf{P}$. This yields to the following model:

$$
\begin{cases}
\rho_s \dfrac{\partial^2 \mathbf{d}_H}{\partial t^2} - \nabla \cdot \mathbf{P}(\mathbf{d}_H T_a(\mathbf{s})) = \mathbf{0} & \text{in } \{\Omega_H^0 \cup \Omega_C^0\} \times (0,T], \quad \text{(A.3a)}\\
\mathbf{P}(\mathbf{d}_H, T_a(\mathbf{s}))\mathbf{N} = \mathbf{K}^{\text{epi}} \mathbf{d}_H + \mathbf{C}^{\text{epi}} \dfrac{\partial \mathbf{d}_H}{\partial t} & \text{on } \Gamma_H^{\text{epi}} \times (0,T], \quad \text{(A.3b)}\\
\mathbf{P}(\mathbf{d}_H, T_a(\mathbf{s}))\mathbf{N} = -p_{\text{LV}}(t)\, J \mathbf{F}^{-T}\mathbf{N} & \text{on } \Gamma^{LV} \times (0,T], \quad \text{(A.3c)}\\
\mathbf{P}(\mathbf{d}_H, T_a(\mathbf{s}))\mathbf{N} = -p_{\text{RV}}(t)\, J_H \mathbf{F}_H^{-T}\mathbf{N} & \text{on } \Gamma^{RV} \times (0,T], \quad \text{(A.3d)}\\
\mathbf{P}(\mathbf{d}_H, T_a(\mathbf{s}))\mathbf{N} & \\
\quad = |J_H \mathbf{F}_H^{-T}\mathbf{N}| \left[p_{\text{LV}}(t)\mathbf{v}_{\text{LV}}^{\text{base}} + p_{\text{RV}}(t)\mathbf{v}_{\text{RV}}^{\text{base}} \right] & \text{on } \Gamma_H^{\text{base}} \times (0,T], \quad \text{(A.3e)}\\
\mathbf{d}_H = \mathbf{d}_{0,H} & \text{in } \{\Omega_H^0 \cup \Omega_C^0\} \times \{t=0\}, \quad \text{(A.3f)}
\end{cases}
$$

where $\mathbf{v}_{\text{LV}}^{\text{base}}$ and $\mathbf{v}_{\text{RV}}^{\text{base}}$ are the following vectors [63]:

$$
\mathbf{v}_i^{\text{base}} = \frac{\int_{\Gamma_H^{\text{endo},i}} J\mathbf{F}_H^{-T}\mathbf{N} d\Gamma_H^i}{\int_{\Gamma_H^{\text{endo},i}} |J\mathbf{F}_H^{-T}\mathbf{N}| d\Gamma_H^i} \qquad i = LV, RV.
$$

The myocardial tissue is assumed to be an hyperelastic material [74,75], while active mechanics is described by means of an active stress approach [76,77]. The Piola–Kirchhoff $\mathbf{P} = \mathbf{P}(\mathbf{d}, T_a)$ stress tensor is decomposed in a first term, representing the strain energy density function $\mathcal{W} : \text{Lin}^+ \to \mathbb{R}$, and a second one corresponding to the orthotropic active stress, namely:

$$
\mathbf{P}(\mathbf{d}_H, T_a) = \frac{\partial \mathcal{W}(\mathbf{F}_H)}{\partial \mathbf{F}_H} + T_a(\hat{\xi}, \mathbf{s}) \left[n_f \frac{\mathbf{F}_H \mathbf{f}_0 \otimes \mathbf{f}_0}{\sqrt{I_{4f}}} + n_n \frac{\mathbf{F}_H \mathbf{n}_0 \otimes \mathbf{n}_0}{\sqrt{I_{4n}}} \right].
$$

Here, $\mathbf{F}_H$ is the deformation tensor, while $T_a(\hat{\xi}, \mathbf{s})$ is the active tension provided by the activation model. $I_{4f} = \mathbf{F}_H \mathbf{f}_0 \cdot \mathbf{F}_H \mathbf{f}_0$ and $I_{4n} = \mathbf{F}_H \mathbf{n}_0 \cdot \mathbf{F}_H \mathbf{n}_0$ represent the tissue stretches along the fiber and sheet-normal directions, respectively, being n_f and n_n the prescribed portion of active stress tensor in fiber and sheet-normal directions.

The strain energy function $\mathcal{W}$ is described by the Guccione constitutive law [74]:

$$
\mathcal{W} = \frac{\kappa}{2}(J-1)\log(J) + \frac{\tilde{a}}{2}(e^Q - 1), \tag{A.4}
$$

where the first term accounts for the volumetric energy, including the bulk modulus κ. The term $\tilde{a}$ is a stiffness scaling parameter $\tilde{a} = a[\mu + (1-\mu)4.56]$, see [59], where μ is the parameter that account for possible scars and gray zones in the myocardium.

In Eq. (A.4), the exponent Q is related to the Green–Lagrange strain tensor $\mathbf{E} = \frac{1}{2}(\mathbf{C} - \mathbf{I})$, being $\mathbf{C} = \mathbf{F}_H^T \mathbf{F}_H$ the right Cauchy–Green deformation tensor, by:

$$
Q = b_{\text{ff}} E_{\text{ff}}^2 + b_{\text{ss}} E_{\text{ss}}^2 + b_{\text{fs}}(E_{\text{fs}}^2 + E_{\text{sf}}^2) + b_{\text{fn}}(E_{\text{fn}}^2 + E_{\text{nf}}^2) + b_{\text{sn}}(E_{\text{sn}}^2 + E_{\text{nf}}^2),
$$

where b is the stiffness scaling parameter and $E_{\text{ij}} = \mathbf{E}\mathbf{i}_0 \cdot \mathbf{j}_0$, for i,j $\in$ {f,s,n} and $\mathbf{i}_0, \mathbf{j}_0 \in \{\mathbf{f}_0, \mathbf{n}_0, \mathbf{s}_0\}$ are the entries of the Green–Lagrange strain tensor $\mathbf{E}$.

Boundary conditions (A.3b)–(A.3e) are prescribed to model the interaction of the endocardium with the blood, as well as the tension due to the continuity of the heart muscle on the base and the pericardium [79–81]. The blood–endocardium interaction is modeled through normal stress boundary conditions (A.3c)–(A.3d) prescribed at the endocardial surface $\Gamma_H^{\text{endo,LV}}$ and $\Gamma_H^{\text{endo,RV}}$ and on the cap surfaces $\Gamma_C^{\text{endo,LV}}$ and $\Gamma_C^{\text{endo,RV}}$. The energy-consistent boundary condition accounting for the effect of the neglected part of the biventricular domain is instead imposed through (A.3e) on Γ_H^{base} (see [62,108]) . Finally, the effect of the pericardium is accounted for by means of generalized Robin boundary conditions at the epicardial surfaces Γ_H^{epi} (A.3b) through the tensors $\mathbf{K}^{\text{epi}} = K_{\parallel}^{\text{epi}}(\mathbf{N} \otimes \mathbf{N} - \mathbf{I}) - K_{\perp}^{\text{epi}}(\mathbf{N} \otimes \mathbf{N})$ and $\mathbf{C}^{\text{epi}} = C_{\parallel}^{\text{epi}}(\mathbf{N} \otimes \mathbf{N} - \mathbf{I}) - C_{\perp}^{\text{epi}}(\mathbf{N} \otimes \mathbf{N})$, with $K_{\perp}^{\text{epi}}$, $C_{\perp}^{\text{epi}}$, $K_{\parallel}^{\text{epi}}$, $C_{\parallel}^{\text{epi}} \in \mathbb{R}^+$ the stiffness and viscosity parameters of the epicardium in normal and tangential directions, respectively.

A.4. Circulation

The role of blood circulation in the cardiac contraction is included by the 0D description of the complete cardiovascular system proposed in [62,63] that models the systemic and the pulmonary circulations as RLC circuits, the heart chambers with time-varying elastance elements, and the heart valves through non-ideal diodes. The resulting ODE system:

$$
\begin{cases}
\dfrac{d\boldsymbol{c}(t)}{dt} = \boldsymbol{D}(t, \boldsymbol{c}(t), p_{\text{LV}}(t), p_{\text{RV}}(t)) & t \in (0,T], \quad \text{(A.5a)}\\
\mathbf{c} = \mathbf{c}_0 & t = 0, \quad \text{(A.5b)}
\end{cases}
$$

represents therefore the blood circulation. Pressures, volumes and fluxes of the different vascular compartments are included in the unknowns vector **c**.

The coupling of the 0D circulatory model with the 3D biventricular model EM model is achieved by replacing the time-varying elastance elements of the LV and RV with their corresponding 3D descriptions in the circulation model. A suitable volume-consistency coupling conditions, given by:

$$V_i^{3D}(\mathbf{c}(t)) = \int_{\Sigma_0^{\text{endo,i}}} J(t)((\mathbf{h}\otimes\mathbf{h})(\mathbf{x}+\mathbf{d}_H(t)-\mathbf{b}_i))\cdot\mathbf{F}^{-T}(t)\mathbf{N}d\Gamma_0, \quad i=\text{LV, RV}$$

is introduced, being **h** an orthogonal vector to the LV and RV centerline, while $\mathbf{b}_i$ is a vector inside the LV and RV. Therefore, pressures of the LV and RV in the 3D–0D coupled model can be determined through the Lagrange multipliers associated to the constraints:

$$\begin{cases} V_{\text{LV}}(\boldsymbol{c}(t)) = V_{\text{LV}}^{\text{3D}}(\mathbf{d}_H(t)) & t\in(0,T], \quad \text{(A.6a)} \\ V_{\text{RV}}(\boldsymbol{c}(t)) = V_{\text{RV}}^{\text{3D}}(\mathbf{d}_H(t)) & t\in(0,T], \quad \text{(A.6b)} \end{cases}$$

rather than via the 0D circulation model.

A.5. 12 lead ECG system

The standard 12-lead ECG is a system of 12 leads obtained by combining the values of u_T recorded from 9 electrodes on the surface of the human body, named R, L, F, and V_i, $i=1,\dots,6$ (referred to Fig. 14 for a representation of the electrodes distribution). Defining by $\mathbf{x}_R$, $\mathbf{x}_L$, $\mathbf{x}_F$, $\mathbf{x}_{V_i}$, the spatial location of the electrodes, the 6 limb leads are computed as:

$$I = u_T(\mathbf{x}_L) - u_T(\mathbf{x}_R), \quad II = u_T(\mathbf{x}_F) - u_T(\mathbf{x}_R), \quad III = u_T(\mathbf{x}_F) - u_T(\mathbf{x}_L),$$
$$aVR = u_T(\mathbf{x}_R) - \frac{1}{2}(u_T(\mathbf{x}_L)+u_T(\mathbf{x}_F)), \quad aVL = u_T(\mathbf{x}_L) - \frac{1}{2}(u_T(\mathbf{x}_R)+u_T(\mathbf{x}_F)),$$
$$aVF = u_T(\mathbf{x}_F) - \frac{1}{2}(u_T(\mathbf{x}_L)+u_T(\mathbf{x}_R)),$$

whereas the 6 precordial (or chest) leads are defined as:

$$V_i = u_T(\mathbf{x}_{V_i}) - WCT, \quad i=1,\dots,6,$$

with WCT denoting the Wilson central terminal signal, given by:

$$WCT = \frac{1}{3}\left[u_T(\mathbf{x}_L)+u_T(\mathbf{x}_R)+u_T(\mathbf{x}_F)\right].$$

References

[1] N.A. Trayanova, K.-C. Chang, How computer simulations of the human heart can improve anti-arrhythmia therapy, J. Physiol. 594 (2016) 2483–2502, http://dx.doi.org/10.1113/JP270532.

[2] S.A. Niederer, J. Lumens, N.A. Trayanova, Computational models in cardiology, Nat. Rev. Cardiol. 16 (2019) 100–111.

[3] J. Corral-Acero, F. Margara, M. Marciniak, C. Rodero, F. Loncaric, Y. Feng, A. Gilbert, J.F. Fernandes, H.A. Bukhari, A. Wajdan, et al., The digital twin to enable the vision of precision cardiology, Eur. Heart J. 41 (2020) 4556–4564.

[4] M. Peirlinck, F.S. Costabal, J. Yao, J. Guccione, S. Tripathy, Y. Wang, D. Ozturk, P. Segars, T. Morrison, S. Levine, et al., Precision medicine in human heart modeling: Perspectives, challenges, and opportunities, Biomech. Model. Mechanobiol. 20 (2021) 803–831.

[5] N.A. Trayanova, A. Prakosa, Up digital and personal: How heart digital twins can transform heart patient care, Heart Rhythm 21 (2024) 89–99, http://dx.doi.org/10.1016/j.hrthm.2023.10.019.

[6] K. Gillette, M.A.F. Gsell, M. Strocchi, T. Grandits, A. Neic, M. Manninger, D. Scherr, C. Roney, A. Prassl, C. Augustin, E. Vigmond, G. Plank, A personalized real-time virtual model of whole heart electrophysiology, EP Europace 25 (2023) euad122.541, http://dx.doi.org/10.1093/europace/euad122.541.

[7] O. Zettinig, T. Mansi, B. Georgescu, E. Kayvanpour, F. Sedaghat-Hamedani, A. Amr, J. Haas, H. Steen, B. Meder, H. Katus, N. Navab, A. Kamen, D. Comaniciu, Fast data-driven calibration of a cardiac electrophysiology model from images and ECG, in: Medical Image Computing and Computer-Assisted Intervention, in: volume 16 of *Part 1*, 2013, pp. 1–8, http://dx.doi.org/10.1007/978-3-642-40811-3_1.

[8] O. Zettinig, T. Mansi, D. Neumann, B. Georgescu, S. Rapaka, P. Seegerer, E. Kayvanpour, F. Sedaghat-Hamedani, A. Amr, J. Haas, H. Steen, H. Katus, B. Meder, N. Navab, A. Kamen, D. Comaniciu, Data-driven estimation of cardiac electrical diffusivity from 12-lead ECG signals, Med. Image Anal. 18 (2014) 1361–1376, http://dx.doi.org/10.1016/j.media.2014.04.011.

[9] T. Grandits, J. Verhü, G. Haase, A. Effland, S. Pezzuto, Digital twinning of cardiac electrophysiology models from the surface ECG: A geodesic backpropagation approach, 2023.

[10] J. Camps, L.A. Berg, Z.J. Wang, R. Sebastian, L.L. Riebel, R. Doste, X. Zhou, R. Sachetto, J. Coleman, B. Lawson, V. Grau, K. Burrage, A. Bueno-Orovio, R. Weber, B. Rodriguez, Digital twinning of the human ventricular activation sequence to clinical 12-lead ECGs and magnetic resonance imaging using realistic Purkinje networks for in silico clinical trials, 2023.

[11] L. Qiao, S. Hu, B. Xiao, X. Bi, W. Li, X. Gao, A dual self-calibrating framework for noninvasive fetal ECG R-peak detection, IEEE Internet Things J. 10 (2023) 16579–16593, http://dx.doi.org/10.1109/JIOT.2023.3269096.

[12] K. Gillette, M.A. Gsell, A.J. Prassl, E. Karabelas, U. Reiter, G. Reiter, T. Grandits, C. Payer, D. Štern, M. Urschler, J.D. Bayer, C.M. Augustin, A. Neic, T. Pock, E.J. Vigmond, G. Plank, A framework for the generation of digital twins of cardiac electrophysiology from clinical 12-leads ECGs, Med. Image Anal. 71 (2021) 102080, http://dx.doi.org/10.1016/j.media.2021.102080.

[13] J.-I. Okada, T. Sasaki, T. Washio, H. Yamashita, T. Kariya, Y. Imai, M. Nakagawa, Y. Kadooka, R. Nagai, T. Hisada, S. Sugiura, Patient specific simulation of body surface ECG using the finite element method, Pacing Clin. Electrophysiol. 36 (2013) 309–321, http://dx.doi.org/10.1111/pace.12057.

[14] Z.J. Wang, A. Santiago, X. Zhou, L. Wang, F. Margara, F. Levrero-Florencio, A. Das, C. Kelly, E. Dall'Armellina, M. Vazquez, B. Rodriguez, Human biventricular electromechanical simulations on the progression of electrocardiographic and mechanical abnormalities in post-myocardial infarction, EP Europace 23 (2021) i143–i152, http://dx.doi.org/10.1093/europace/euaa405.

[15] A. Lopez-Perez, R. Sebastian, M. Izquierdo, R. Ruiz, M. Bishop, J.M. Ferrero, Personalized cardiac computational models: From clinical data to simulation of infarct-related ventricular tachycardia, Front. Physiol. 10 (2019) 580.

[16] J. Relan, P. Chinchapatnam, M. Sermesant, K. Rhode, M. Ginks, H. Delingette, C.A. Rinaldi, R. Razavi, N. Ayache, Coupled personalization of cardiac electrophysiology models for prediction of ischaemic ventricular tachycardia, Interface Focus 1 (2011) 396–407, http://dx.doi.org/10.1098/rsfs.2010.0041, https://royalsocietypublishing.org/doi/abs/10.1098/rsfs.2010.0041.

[17] J. Bergquist, L. Rupp, B. Zenger, J. Brundage, A. Busatto, R.S. MacLeod, Body surface potential mapping: Contemporary applications and future perspectives, Hearts 2 (2021) 514–542, http://dx.doi.org/10.3390/hearts2040040, https://www.mdpi.com/2673-3846/2/4/40.

[18] Z.F. Issa, J.M. Miller, D.P. Zipes, 6 - advanced mapping and navigation modalities, in: Z.F. Issa, J.M. Miller, D.P. Zipes (Eds.), Clinical Arrhythmology and Electrophysiology (Third Edition), third ed., Elsevier, Philadelphia, 2019, pp. 155–205, http://dx.doi.org/10.1016/B978-0-323-52356-1.00006-2.

[19] Y. Feng, C. Roney, J. Bayer, S. Niederer, M. Hocini, V. E.J., Detection of focal source and arrhythmogenic substrate from body surface potentials to guide atrial fibrillation ablation, PLoS Comput. Biol. 18 (2022) http://dx.doi.org/10.1371/journal.pcbi.1009893.

[20] V.G. Marques, M. Rodrigo, M. de la Salu. Guillem, J. Salinet, Characterization of atrial arrhythmias in body surface potential mapping: A computational study, Comput. Biol. Med. 127 (2020) 103904, http://dx.doi.org/10.1016/j.compbiomed.2020.103904.

[21] A. Ferrer, R. Sebastian, J.F. Rodriguez, C. Tobón, M. Guillem, E.J. Godoy, J. Saiz, Computational simulation and analysis of 3D body surface potential patterns generated by common atrial arrhythmias, Comput. Cardiol. 2013 (2013) 919–922.

[22] N. Zemzemi, M.O. Bernabeu, J. Saiz, J. Cooper, P. Pathmanathan, G.R. Mirams, J. Pitt-Francis, B. Rodriguez, Computational assessment of drug-induced effects on the electrocardiogram: From ion channel to body surface potentials, Bri. J. Pharmacol. 168 (2013) 718–733, http://dx.doi.org/10.1111/j.1476-5381.2012.02200.x.

[23] A. Pullan, M. Buist, L. Cheng, Mathematically modelling the electrical activity of the heart: From cell to body surface and back again, 2005, http://dx.doi.org/10.1142/9789812775153.

[24] J. Malmivuo, R. Plonsey, Bioelectromagnetism - principles and applications of bioelectric and biomagnetic fields, 1995, http://dx.doi.org/10.1093/acprof:oso/9780195058239.001.0001.

[25] R.S. MacLeod, R.L. Lux, B. Taccardi, A possible mechanism for electrocardiographically silent changes in cardiac repolarization, J. Electrocardiol. 30 (1998) 114–121, http://dx.doi.org/10.1016/S0022-0736(98)80053-8.

[26] R. Andlauer, G. Seemann, L. Baron, O. Dössel, P. Kohl, P. Platonov, A. Loewe, Influence of left atrial size on P-wave morphology: Differential effects of dilation and hypertrophy, EP Europace 20 (2018) http://dx.doi.org/10.1093/europace/euy231.

[27] B.J. Schijvenaars, G. van Herpen, J.A. Kors, Intraindividual variability in electrocardiograms, J. Electrocardiol. 41 (2008) 190–196, http://dx.doi.org/10.1016/j.jelectrocard.2008.01.012.

[28] G.J.M. Huiskamp, A. van Oosterom, Heart position and orientation in forward and inverse electrocardiography, Med. Biol. Eng. Comput. 30 (2006) 613–620.

[29] U.C. Nguyên, M. Potse, F. Regoli, M.L. Caputo, G. Conte, R. Murzilli, S. Muzzarelli, T. Moccetti, E.G. Caiani, F.W. Prinzen, R. Krause, A. Auricchio, An in-silico analysis of the effect of heart position and orientation on the ECG morphology and vectorcardiogram parameters in patients with heart failure and intraventricular conduction defects, J. Electrocardiol. 48 (2015) 617–625, http://dx.doi.org/10.1016/j.jelectrocard.2015.05.004.

[30] A. Mincholé, E. Zacur, R. Ariga, V. Grau, B. Rodriguez, MRI-based computational torso/biventricular multiscale models to investigate the impact of anatomical variability on the ECG QRS complex, Front. Physiol. 10 (2019) http://dx.doi.org/10.3389/fphys.2019.01103.

[31] T. Feldman, R. Childers, K. Borow, K. Lang, A. Neumann, Change in ventricular cavity size: Differential effects on QRS and T wave amplitude, Circulation 72 (1985) 495–501, http://dx.doi.org/10.1161/01.CIR.72.3.495.

[32] C. Nagel, S. Schuler, O. Dössel, A. Loewe, A bi-atrial statistical shape model for large-scale in silico studies of human Atria: Model development and application to ECG simulations, Med. Image Anal. 74 (2021) 102210, http://dx.doi.org/10.1016/j.media.2021.102210.

[33] E. Zappon, A. Manzoni, A. Quarteroni, A staggered-in-time and non-conforming-in-space numerical framework for realistic cardiac electrophysiology outputs, 2023.

[34] S. Nat. Poltri, G. Caluori, P. Jaïs, A. Collin, C. Poignard, Electrocardiology modeling after catheter ablations for atrial fibrillation, in: O. Bernard, P. Clarysse, N. Duchateau, J. Ohayon, M. Viallon (Eds.), Functional Imaging and Modeling of the Heart, Springer Nature Switzerland, Cham, 2023, pp. 184–193.

[35] P. Colli-Franzone, L. Pavarino, S. Scacchi, Mathematical Cardiac Electrophysiology, vol. 13, Springer, 2014.

[36] A. Quarteroni, L. Dedè, A. Manzoni, C. Vergara, Mathematical Modelling of the Human Cardiovascular System: Data, Numerical Approximation, Clinical Applications, Cambridge Monographs on Applied and Computational Mathematics, Cambridge University Press, 2019.

[37] J. Sundnes, G. Lines, X. Cai, B. Nielsen, K. Mardal, A. Tveito, Computing the electrical activity in the human heart, 2006, http://dx.doi.org/10.1007/3-540-33437-8.

[38] L. Gander, R. Krause, M. Weiser, F. Costabal, S. Pezzuto, On the accuracy of eikonal approximations in cardiac electrophysiology in the presence of fibrosis, in: Functional Imaging and Modeling of the Heart, FIMH 2023, 2023, p. 13958, http://dx.doi.org/10.1007/978-3-031-35302-4_14.

[39] S. Stella, F. Regazzoni, C. Vergara, L. Dedé, A. Quarteroni, A fast cardiac electromechanics model coupling the Eikonal and the nonlinear mechanics equations, Math. Models Methods Appl. Sci. 32 (2022) 1531–1556, http://dx.doi.org/10.1142/S021820252250035X.

[40] E. Konukoglu, J. Relan, U. Cilingir, B.H. Menze, P. Chinchapatnam, A. Jadidi, H. Cochet, M. Hocini, H. Delingette, P. Jaïs, M. Haïssaguerre, N. Ayache, M. Sermesant, Efficient probabilistic model personalization integrating uncertainty on data and parameters: Application to Eikonal-diffusion models in cardiac electrophysiology, Prog. Biophys. Mol. Biol. 107 (2011) 134–146, http://dx.doi.org/10.1016/j.pbiomolbio.2011.07.002, experimental and Computational Model Interactions in Bio-Research: State of the Art.

[41] A. Neic, F.O. Campos, A.J. Prassl, S.A. Niederer, M.J. Bishop, E.J. Vigmond, G. Plank, Efficient computation of electrograms and ECGs in human whole heart simulations using a reaction-Eikonal model, J. Comput. Phys. 346 (2017) 191–211.

[42] M. Multerer, S. Pezzuto, Uncertainty quantification for the 12-lead ECG: A lead field approach, 2021, arXiv preprint arXiv:2102.09960.

[43] M. Potse, Scalable and accurate ECG simulation for reaction-diffusion models of the human heart, Front. Physiol. 9 (2018) http://dx.doi.org/10.3389/fphys.2018.00370.

[44] M. Boulakia, S. Cazeau, M. Fernández, J. Gerbeau, N. Zemzemi, Mathematical modeling of electrocardiograms: A numerical study, Ann. Biomed. Eng. 38 (2010) 1071–1097, http://dx.doi.org/10.1007/s10439-009-9873-0.

[45] M. Potse, B. Dubé, A. Vinet, Cardiac anisotropy in boundary-element models for the electrocardiogram, Med. Biol. Eng. Comput. 47 (2009) 719–729, http://dx.doi.org/10.1007/s11517-009-0472-x.

[46] M. Aoki, Y. Okamoto, T. Musha, K.-I. Harumi, Three-dimensional simulation of the ventricular depolarization and repolarization processes and body surface potentials: Nornal heart and bundle branch block, IEEE Trans. Biomed. Eng. BME-34 (1987) 454–462, http://dx.doi.org/10.1109/TBME.1987.326079.

[47] K.A. Sedova, P.M. van Dam, M. Blahova, et al., Localization of the ventricular pacing site from BSPM and standard 12-lead ECG: A comparison study, Sci. Rep. 13 (2023) 9618, http://dx.doi.org/10.1038/s41598-023-36768-z.

[48] M. Potse, B. Dubé, A. Vinet, Cardiac anisotropy in boundary-element models for the electrocardiogram, Med. Biol. Eng. Comput. 47 (2009) 719–729, http://dx.doi.org/10.1007/s11517-009-0472-x.
[49] M. Fuchs, M. Wagner, J. Kastner, Boundary element method volume conductor models for EEG source reconstruction, Clin. Neurophysiol. 112 (2001) 1400–1407, http://dx.doi.org/10.1016/S1388-2457(01)00589-2.
[50] D.B. Geselowitz, On bioelectric potentials in an inhomogeneous volume conductor, Biophys. J. 7 (1967) 1–11.
[51] B.L. de Oliveira, B.M. Rocha, L.P.S. Barra, E.M. Toledo, J. Sundnes, R.W. dos Santos, Effects of deformation on transmural dispersion of repolarization using in silico models of human left ventricular wedge, Int. J. Numer. Methods Biomed. Eng. 29 (2013) 1323–1337, http://dx.doi.org/10.1002/cnm.2570.
[52] M. Favino, S. Pozzi, S. Pezzuto, F. Prinzen, A. Auricchio, R. Krause, Impact of mechanical deformation on pseudo-ECG: A simulation study, Europace 18 (2016) iv77–iv84, http://dx.doi.org/10.1093/europace/euw353.
[53] N.P. Smith, M.L. Buist, A.J. Pullan, Altered T wave dynamics in a contracting cardiac model, J. Cardiovasc. Electrophysiol. 14 (2003).
[54] D.U.J. Keller, O. Jarrousse, T. Fritz, S. Ley, O. Dössel, G. Seemann, Impact of physiological ventricular deformation on the morphology of the T-wave: A hybrid, static-dynamic approach, Trans. Biomed. Eng. 58 (2011) 2109–2119, http://dx.doi.org/10.1109/TBME.2011.2147785.
[55] Q. Wei, F. Liu, B. Appleton, L. Xia, N. Liu, S. Wilson, R. Riley, W. Strugnel, R. Slaughter, R. Denman, S. Crozier, Effect of cardiac motion on body surface electrocardiographic potentials: An MRI-based simulation study, Phys. Med. Biol. 51 (2006) 3405–3418, http://dx.doi.org/10.1088/0031-9155/51/14/009.
[56] L. Xia, M. Huo, Q. Wei, F. Liu, S. Crozier, Analysis of cardiac ventricular wall motion based on a three-dimensional electromechanical biventricular model, Phys. Med. Biol. 50 (2005) 1901–1917, http://dx.doi.org/10.1088/0031-9155/50/8/018.
[57] R. Moss, E.M. Wülfers, S. Schuler, A. Loewe, G. Seemann, A fully-coupled electro-mechanical whole-heart computational model: Influence of cardiac contraction on the ECG, Front. Physiol. 12 (2021) http://dx.doi.org/10.3389/fphys.2021.778872.
[58] M. Salvador, F. Regazzoni, S. Pagani, L. Dede', N. Trayanova, A. Quarteroni, The role of mechano-electric feedbacks and hemodynamic coupling in scar-related ventricular Tachycardia, Comput. Biol. Med. 142 (2022) 105203, http://dx.doi.org/10.1016/j.compbiomed.2021.105203.
[59] M. Salvador, M. Fedele, P.C. Africa, E. Sung, L. Dede', A. Prakosa, J. Chrispin, N. Trayanova, A. Quarteroni, Electromechanical modeling of human ventricles with ischemic cardiomyopathy: Numerical simulations in sinus rhythm and under arrhythmia, Comput. Biol. Med. 136 (2021) 104674, http://dx.doi.org/10.1016/j.compbiomed.2021.104674.
[60] M. Peirlinck, J. Yao, F. Sahl Costabal, E. Kuhl, How drugs modulate the performance of the human heart, Comput. Mech. 69 (2022) 1397–1411.
[61] M. Fedele, R. Piersanti, F. Regazzoni, M. Salvador, P.C. Africa, M. Bucelli, A. Zingaro, L. Dede', A. Quarteroni, A comprehensive and biophysically detailed computational model of the whole human heart electromechanics, Comput. Methods Appl. Mech. Engrg. 410 (2023) 115983, http://dx.doi.org/10.1016/j.cma.2023.115983.
[62] R. Piersanti, F. Regazzoni, M. Salvador, A.F. Corno, L. Dede', C. Vergara, A. Quarteroni, 3D–0D closed-loop model for the simulation of cardiac biventricular electromechanics, Comput. Methods Appl. Mech. Engrg. 391 (2022) 114607, http://dx.doi.org/10.1016/j.cma.2022.114607.
[63] F. Regazzoni, M. Salvador, P. Africa, M. Fedele, L. Dedé, A. Quarteroni, A cardiac electromechanical model coupled with a lumped-parameter model for closed-loop blood circulation, J. Comput. Phys. 457 (2022) 111083, http://dx.doi.org/10.1016/j.jcp.2022.111083.
[64] Official lifex website, 2023, https://lifex.gitlab.io/. (Accessed: 15 June 2023).
[65] P.C. Africa, R. Piersanti, F. Regazzoni, M. Bucelli, M. Salvador, M. Fedele, S. Pagani, L. Dede', A. Quarteroni, Lifex-ep: A robust and efficient software for cardiac electrophysiology simulations, BMC Bioinform. 24 (2023) 389, http://dx.doi.org/10.1186/s12859-023-05513-8.
[66] P.C. Africa, R. Piersanti, M. Fedele, L. Dede, A. Quarteroni, Lifex-fiber: An open tool for myofibers generation in cardiac computational models, BMC Bioinformatics 24 (2022) http://dx.doi.org/10.1186/s12859-023-05260-w.
[67] K. ten Tusscher, A. Panfilov, Alternans and spiral breakup in a human ventricular tissue model, Am. J. Physiol.-Heart Circul. Physiol. 291 (2006) H1088–H1100.
[68] R. Piersanti, P. Africa, M. Fedele, C. Vergara, L. Dedè, A. Corno, A. Quarteroni, Modeling cardiac muscle fibers in ventricular and atrial electrophysiology simulations, Comput. Methods Appl. Mech. Engrg. 373 (2021) 113468.
[69] D. Durrer, R. Va. Dam, G. Freud, M. Janse, F. Meijler, R. Arzbaecher, Total excitation of the isolated human heart, Circulation 41 (1970) 899–912.
[70] R. Myerburg, H. Gelband, K. Nilsson, A. Castellanos, A. Morales, A. Bassett, The role of canine superficial ventricular muscle fibers in endocardial impulse distribution, Circ. Res. 42 (1978) 27–35, http://dx.doi.org/10.1161/01.RES.42.1.27.
[71] P. Colli-Franzone, L. Pavarino, S. Scacchi, A numerical study of scalable cardiac electro-mechanical solvers on HPC architectures, Front. Physiol. 9 (2018) 268.
[72] F. Regazzoni, L. Dedè, A. Quarteroni, Biophysically detailed mathematical models of multiscale cardiac active mechanics, PLoS Comput. Biol. 16 (2020) e1008294.
[73] M. Fedele, A. Quarteroni, Polygonal surface processing and mesh generation tools for the numerical simulation of the cardiac function, Int. J. Numer. Methods Biomed. Eng. 37 (2021) e3435.
[74] J. Guccione, A. McCulloch, Finite element modeling of ventricular mechanics, in: Theory of Heart, Springer, 1991, pp. 121–144.
[75] R. Ogden, Non-Linear Elastic Deformations, Courier Corporation, 1997.
[76] S. Göktepe, E. Kuhl, Electromechanics of the heart: A unified approach to the strongly coupled excitation–contraction problem, Comput. Mech. 45 (2010) 227–243.
[77] N. Smith, D. Nickerson, E. Crampin, P. Hunter, Multiscale computational modelling of the heart, Acta Numer. 13 (2004) 371.
[78] J. Guccione, A. McCulloch, L. Waldman, Passive material properties of intact ventricular myocardium determined from a cylindrical model, J. Biomech. Eng. 113 (1991) 42–55.
[79] A. Gerbi, L. Dedè, A. Quarteroni, A monolithic algorithm for the simulation of cardiac electromechanics in the human left ventricle, Math. Eng. 1 (2018) 1–37.
[80] M. Pfaller, J. Hörmann, M. Weigl, A. Nagler, R. Chabiniok, C. Bertoglio, W. Wall, The importance of the pericardium for cardiac biomechanics: From physiology to computational modeling, Biomech. Model. Mechanobiol. 18 (2019) 503–529.
[81] M. Strocchi, M. Gsell, C. Augustin, O. Razeghi, C. Roney, A. Prassl, E. Vigmond, J. Behar, J. Gould, C. Rinaldi, et al., Simulating ventricular systolic motion in a four-chamber heart model with spatially varying Robin boundary conditions to model the effect of the pericardium, J. Biomech. 101 (2020) 109645.
[82] H. Arevalo, F. Vadakkumpadan, E. Guallar, A. Jebb, P. Malamas, K. Wu, N. Trayanova, Arrhythmia risk stratification of patients after myocardial infarction using personalized heart models, Nat. Commun. 7 (2016) 11437, http://dx.doi.org/10.1038/ncomms11437.
[83] A. Johnson, T. Tezduyar, Mesh update strategies in parallel finite element computations of flow problems with moving boundaries and interfaces, Comput. Methods Appl. Mech. Engrg. 119 (1994) 73–94, http://dx.doi.org/10.1016/0045-7825(94)00077-8.
[84] K. Stein, T. Tezduyar, R. Benney, Mesh moving techniques for fluid-structure interactions with large displacements, J. Appl. Mech. 70 (2003) 58–63, http://dx.doi.org/10.1115/1.1530635.
[85] P. Coll Franzone, L.F. Pavarino, S. Scacchi, Bioelectrical effects of mechanical feedbacks in a strongly coupled cardiac electro-mechanical model, Math. Models Methods Appl. Sci. 26 (2016) 27–57.
[86] F. Regazzoni, A. Quarteroni, Accelerating the convergence to a limit cycle in 3D cardiac electromechanical simulations through a data-driven 0D emulator, Comput. Biol. Med. (2021) 104641.
[87] A. Quarteroni, R. Sacco, F. Saleri, Numerical mathematics, vol. 37, Springer Science & Business Media, 2010.
[88] S. Niederer, L. Mitchell, N. Smith, G. Plank, Simulating human cardiac electrophysiology on clinical time-scales, Front. Physiol. 2 (2011) 14.

[89] T. Hughes, The Finite Element Method: Linear Static and Dynamic Finite Element Analysis, Courier Corporation, 2021.
[90] A. Quarteroni, Numerical Models for Differential Problems, vol. 2, Springer, 2009.
[91] P. Africa, M. Salvador, P. Gervasio, L. Dede', A. Quarteroni, A matrix-free high-order solver for the numerical solution of cardiac electrophysiology, J. Comput. Phys. 478 (2023) 111984, http://dx.doi.org/10.1016/j.jcp.2023.111984.
[92] Z.M.G. Inc, Zygote Solid 3d Heart Generation II Developement Report, Technical Report, 2014.
[93] A. Ferrer, R. Sebastián, D. Sánchez-Quintana, J. Rodríguez, E. Godoy, L. Martínez, J. Saiz, Detailed anatomical and electrophysiological models of human atria and torso for the simulation of atrial activation, PLOS ONE 10 (2015) 1–29, http://dx.doi.org/10.1371/journal.pone.0141573.
[94] Official website of the center for integrative biomedical computing, 2023, https://www.sci.utah.edu/cibc.html (accessed: 15 June 2023).
[95] L. Antiga, M. Piccinelli, L. Botti, B. Ene-Iordache, A. Remuzzi, D. Steinman, An image-based modeling framework for patient-specific computational hemodynamics, Med. Biol. Eng. Comput. 46 (2008) 1097–1112.
[96] Official paraview website, 2023, www.paraview.org. (Accessed: 15 JUne 2023).
[97] A. Frontera, S. Pagani, L.R. Limite, A. Hadjis, A. Manzoni, L. Dedé, A. Quarteroni, P. Della Bella, Outer loop and isthmus in ventricular Tachycardia circuits: Characteristics and implications, Heart Rhythm 17 (2020) 1719–1728, http://dx.doi.org/10.1016/j.hrthm.2020.05.034, https://www.sciencedirect.com/science/article/pii/S1547527120305324.
[98] P.C. Africa, Life^x: A flexible, high performance library for the numerical solution of complex finite element problems, SoftwareX 20 (2022) 101252, http://dx.doi.org/10.1016/j.softx.2022.101252, https://www.sciencedirect.com/science/article/pii/S2352711022001704.
[99] D. Arndt, W. Bangerth, T. Clevenger, D. Davydov, M. Fehling, D. Garcia-Sanchez, G. Harper, T. Heister, L. Heltai, M. Kronbichler, R. Kynch, M. Maier, J.-P. Pelteret, B. Turcksin, D. Wells, The deal.II library version 9.1, J. Numer. Math. (2019).
[100] T. Gerach, S. Schuler, J. Fröhlich, L. Lindner, E. Kovacheva, R. Moss, E.M. Wülfers, G. Seemann, C. Wieners, A. Loewe, Electro-mechanical whole-heart digital twins: A fully coupled multi-physics approach, Mathematics 9 (2021) http://dx.doi.org/10.3390/math9111247.
[101] M. Strocchi, C. Augustin, M. Gsell, E. Karabelas, A. Neic, K. Gillette, O. Razeghi, A. Prassl, E. Vigmond, J. Behar, et al., A publicly available virtual cohort of four-chamber heart meshes for cardiac electro-mechanics simulations, PLoS One 15 (2020) e0235145.
[102] D. Keller, F. Weber, G. Seemann, O. Dössel, Ranking the influence of tissue conductivities on forward-calculated ECGs, IEEE Trans. Bio-Med. Eng. 57 (2010) 1568–1576, http://dx.doi.org/10.1109/TBME.2010.2046485.
[103] C. Sá, G. D'Ambrosio, F. Maffessanti, E. Caiani, F. Prinzen, R. Krause, A. Auricchio, M. Potse, Sensitivity analysis of ventricular activation and electrocardiogram in tailored models of heart-failure patients, Med. Biol. Eng. Comput. 56 (2018) 491–504, http://dx.doi.org/10.1007/s11517-017-1696-9.
[104] K. Holst, M. Ugander, A. Sigfridsson, Respiratory variation in left ventricular cardiac function with 3d double golden-angle whole-heart cine imaging, Magn. Reson. Med. 79 (2018) 2693–2701.
[105] G. Claessen, P. Claus, M. Delcroix, J. Bogaert, A.L. Gerche, H. Heidbuchel, Interaction between respiration and right versus left ventricular volumes at rest and during exercise: A real-time cardiac magnetic resonance study, Am. J. Physiol.-Heart Circul. Physiol. 306 (2014) H816–H824.
[106] G. Shechter, C. Ozturk, J. Resar, E. McVeigh, Respiratory motion of the heart from free breathing coronary angiograms, IEEE Trans. Med. Imaging 23 (2004) 1046–1056, http://dx.doi.org/10.1109/TMI.2004.828676.
[107] F. Regazzoni, L. Dedè, A. Quarteroni, Active contraction of cardiac cells: A reduced model for sarcomere dynamics with cooperative interactions, Biomech. Model. Mechanobiol. 17 (2018) 1663–1686.
[108] F. Regazzoni, L. Dedè, A. Quarteroni, Machine learning of multiscale active force generation models for the efficient simulation of cardiac electromechanics, Comput. Methods Appl. Mech. Engrg. 370 (2020) 113268.